Assessing the ability of the ECMWF seasonal prediction model to forecast extreme September-to-November rainfall events over Equatorial Africa

Hermann N. Nana[1*] · Roméo S. Tanessong[2,1] · Masilin Gudoshava[3] · Derbetini A. Vondou[1]

[1]Laboratory for Environmental Modelling and Atmospheric Physics (LEMAP), Physics Department, University of Yaounde 1, PO Box 812, Yaounde (Cameroon)

[2]Department of Meteorology and Climatology; Higher Institute of Agriculture, Forestry, Water and Environment; University of Ebolowa, PO Box 118, Ebolowa (Cameroon)

[3]IGAD Climate Prediction and Applications Centre (ICPAC), Nairobi, (Kenya)

* Corresponding author: Hermann N. Nana (nanahermann100@yahoo.com)

Hermann N. Nana's orcid: https://orcid.org/0000-0002-0973-8613

Roméo S. Tanessong's orcid: https://orcid.org/0000-0003-3804-5901

Masilin Gudoshava's orcid: https://orcid.org/0000-0003-0315-9271

Derbetini A. Vondou's orcid: https://orcid.org/0000-0002-8681-5328

Abstract

This study investigates the predictability of rainfall over Equatorial Africa (EA) and evaluates the forecasting performance of the European Centre for Medium-Range Weather Forecasts fifth-generation seasonal forecast version 5.1 (ECMWF-SEAS5.1) for the September–November (SON) period during 1981–2023 (43 years). The analysis considers two lead-times, focusing on initial conditions (ICs) from September and August. Regression, spatiotemporal and composite analyses are applied to highlight the relationship between extreme precipitation events over EA and the various associated atmospheric circulation drivers. The analysis reveals that ECMWF-SEAS5.1 successfully reproduces the observed annual precipitation cycle and seasonal spatial pattern of rainfall over the region for both ICs, with notably better skills for September. In addition, the model effectively captures the teleconnections between EA rainfall and tropical sea surface temperature, including the Indian Ocean dipole and El Niño-Southern Oscillation, for both ICs. Regions with highest potential predictability skills coincide with regions where the model accurately represents strong (weak) composite rainfall anomalies, associated with strong (weak) moisture flux convergence (divergence) values, although the magnitude tends to be underestimated. However, other important observed features, such as the components of the African easterly jet, are well represented by the model for the September IC, but not for August. While many atmospheric mechanisms driving precipitation in the region are well simulated, their underestimation likely explains the model's general tendency to underestimate the magnitude of extreme rainfall events. The results of this study support efforts to improve forecast outputs in the national weather services across the region by integrating ECMWF model outputs into operational weather bulletins.

Keywords: Equatorial Africa rainfall, Seasonal forecasting, ENSO, IOD, forecast Skill

1. Introduction

Equatorial Africa (EA) exhibits a complex annual rainfall cycle shaped by the seasonal migration of the Intertropical Convergence Zone (ITCZ), local convection, and moisture transport from the Atlantic and Indian Oceans. Among the different seasons, September to November (SON) is particularly important, as it marks one of the peak rainfall periods for many EA countries and is frequently associated with severe hydrometeorological hazards such as floods and landslides (Moihamette et al., 2024; Gudoshava et al., 2022a; Kenfack et al., 2025; Nana et al., 2025). Understanding and predicting SON rainfall variability is therefore critical for risk preparedness and climate-sensitive planning across the region. The SON rainfall system in EA is influenced by a combination of local, regional, and large-scale drivers. Local factors include mesoscale convective systems and interactions between topography and atmospheric flow (Pokam et al., 2013). Regional circulation patterns, particularly over the eastern equatorial Atlantic and western Indian Ocean, further modulate moisture availability (Kuete et al., 2019; Longandjo and Rouault, 2020). At larger scales, Sea Surface Temperature (SST) variability in the Pacific, Indian, and Atlantic oceans plays a central role in shaping interannual rainfall anomalies (Pokam et al., 2014; Nicholson, 2015). In particular, El Niño Southern Oscillation (ENSO), the Indian Ocean Dipole (IOD), and Atlantic SST anomalies have been shown to influence SON precipitation extremes across EA (Preethi et al., 2015; Roy et al., 2024; Palmer et al., 2023; Nana et al., 2025). Years characterised by the co-occurrence of a positive IOD and strong El Niño such as 1997 and 2023 have produced widespread heavy rainfall over several EA regions (Okoola et al., 2008; Nana et al., 2025). These links underscore the importance of accurately capturing SST-driven teleconnections and associated atmospheric circulation patterns when forecasting SON rainfall.

Despite advances in global numerical weather prediction systems, forecasting SON precipitation over EA remains a persistent challenge. Sparse observational networks, limited understanding of regional climate dynamics, and model-specific errors contribute to substantial uncertainties in seasonal forecasts (Tanessong et al., 2017). While several studies have evaluated the skill of general circulation models over EA (e.g., Feudjio et al., 2022; Nana et al., 2024; Tanessong et al., 2024), important gaps remain particularly regarding the model's ability to reproduce SON extreme rainfall events and their associated large-scale drivers. Most existing evaluations focus on earlier SEAS5 versions or on mechanisms relevant to other seasons (e.g., MAM or JJAS), thus providing an incomplete picture of SON dynamics. These studies found that EA rainfall variability is mainly associated with several factors, including easterly and westerly waves, tropical cyclones, the Madden-Julian Oscillation (MJO) and sea surface temperature (SST) in the Atlantic, Indian and Pacific oceans. For example, Nana et al. (2024) demonstrated that the ability of seasonal forecast models to predict rainfall anomalies occurring over western EA during extreme South Atlantic Ocean Dipole (SAOD) events depends on their skill in forecasting the relationship between rainfall and SAOD, which decreases with increasing lead-time. Their results showed that the ECMWF seasonal forecast system 5 (SEAS5) model best captures this relationship and

the associated rainfall anomalies, a finding also supported by Gebrechorkos et al. (2022). Similarly, Mwangi et al. (2014) evaluated SEAS5 products against data from ten East African stations and found significant forecasting skill for both rainy seasons, with better performance in October–December (OND) compared to March–May (MAM). The ability of the SEAS5 model to simulate the drivers of extreme rainfall during MAM 2018–2020 over eastern EA has been analysed by Gudoshava et al. (2024). The findings of this study indicate that the heavy rainfall events of March–May 2018 and 2020 coincided with an active MJO (Phases 1–4) or a tropical cyclone east of Madagascar. In contrast, the low rainfall observed during the same period in 2019 was linked to tropical cyclones west of Madagascar. Their study also concluded that underestimation of these extreme rainfall intensities was linked to inaccurate MJO forecasts and errors in tropical cyclone location and intensity. For the June–September (JJAS) season, the findings of Ehsan et al. (2022) establish that the spatial and temporal patterns of observed EA rainfall variability, as well as the key climatic features that drive EA precipitation excesses and deficits, are successfully captured by the SEAS5 model, when initialised in May and April. Recent analyses have begun to examine the role of large-scale climate modes in shaping extreme SON rainfall, but few studies have assessed how well seasonal forecast systems capture both the rainfall anomalies and the underlying physical mechanisms. For example, Tefera et al. (2025) showed that SEAS5 is able to capture hydroclimatic extremes linked to coupled IOD-ENSO modes during the first two lead-times, but their assessment did not consider the most recent ECMWF system nor did it explicitly evaluate the associated atmospheric circulation patterns during SON. This gap limits our understanding of the forecast system's ability to represent the processes driving extreme rainfall variability during this crucial season.

Motivated by these limitations, the present study evaluates the performance of the latest ECMWF seasonal forecasting system, SEAS5.1 (Johnson et al., 2019), in simulating SON extreme rainfall events over EA using forecasts initialised in August and September. However, considering that the main difference between SEAS5 and SEAS5.1 is rooted in the interpolation and additional variables (see section 2.1), rather than a change in the physics, dynamics or data assimilation of the model, therefore, no relevant differences in terms of performance between both versions are expected. SEAS5.1 was selected due to its demonstrated skill in representing key global climate teleconnections such as ENSO and the IOD (Nana et al., 2024; Tefera et al., 2025), which exert strong influence on SON precipitation over EA. In addition to providing an updated assessment of model skill, our study explicitly examines the large-scale physical mechanisms SST anomalies, moisture transport, zonal and Walker circulations that accompany extreme rainfall events. This dual approach offers a more comprehensive and physically grounded evaluation than previous studies, thereby contributing toward improved understanding and prediction of SON rainfall extremes in EA. Extreme rainfall events are among the most impactful climate hazards over EA, often leading to severe flooding, infrastructure damage, and socio-economic losses, yet their predictability at seasonal timescales remains limited. Understanding whether a state-of-the-art seasonal forecast system can realistically represent the large-scale

drivers of these extremes is therefore essential. The remainder of the paper is structured as follows. Section 2 describes the SEAS5.1 model, the observational and reanalysis datasets, and the methodology. Section 3 presents the skill assessment of SEAS5.1. Section 4 focuses on rainfall composites and associated SST patterns during extreme SON years, and Section 5 analyses the corresponding atmospheric circulation features. Section 6 concludes the study.

2. Data and methods

2.1. SEAS5.1 re-forecast and observational datasets

In this study, we use re-forecast data from version 5.1 of the ECMWF seasonal prediction system (SEAS5.1), initiated on the 1st of September or the 1st of August for the period 1981-2016, with 25 ensemble members. Our analysis focuses on the September-November (SON) season, considering two initial conditions (ICs): September 1st (L0) and August 1st (L1). This means that the forecasts initialised in September correspond to L1 and L2 for October and November, respectively. Similarly, the August initial conditions indicate that forecasts were initialised in August; therefore, the forecasts for September, October, and November correspond to L1, L2, and L3, respectively. The method used to extract lead-times is consistent with that adopted by Ehsan et al. (2021). With this definition, the initial conditions have a relatively limited influence on the model outputs across the different analyses, especially when compared to the dominant predictive role of oceanic conditions. Monthly mean data are used throughout. It is important to specify that SEAS5.1 initialisations for all the months (not only August and September) were used in order to study the rainfall annual cycle (shown in Fig. 1). To extend the study period, we include forecasts for 2017-2023, using the first 25 ensemble members with the same initialization dates, ensuring each sub-period contributes equally to the analysis. This results in a total of 43 years (1981-2023), with 25 ensemble members per year. A comprehensive explanation of the ensemble generation strategy of the ECMWF's fifth generation seasonal forecast system can be found in Johnson et al. (2019). These data are available from the Copernicus Climate Data Store portal (https://climate.copernicus.eu/datasets) at a spatial resolution of 1° × 1°. The data include monthly means of total precipitation (mm day^{-1}), SST (K), Mean-Sea-Level Pressure (MSLP; hPa), zonal and meridional wind components (m s^{-1}), and specific humidity (Kg Kg^{-1}) at seven pressure levels (1000, 925, 850, 700, 500, 400, and 300 hPa). All the seasonal forecast data used in this study are from SEAS5.1. Although SEAS5.1 replaced SEAS5 operationally in November 2022, the full dataset analyzed here (including the 1981–2021 period) corresponds to the reprocessed SEAS5.1 version. SEAS5.1 differs from the original SEAS5 mainly through the adoption of a new interpolation tool and a revised 1° grid (in the Copernicus Climate Data Store portal) with half-degree–centred latitude/longitude points, ensuring consistency with other Copernicus Climate Change Service seasonal forecast systems. SEAS5.1 also provides an extended set of variables, including top solar incoming radiation, additional fields at

the 1000 hPa pressure level, and separate surface and sub-surface runoff components. The underlying model physics remains unchanged between the two versions.

As precipitation reference in this study, observed monthly precipitation data from the Climate Hazards Group Infrared Precipitation with Station data (CHIRPS; Funk et al., 2015) at 0.25° × 0.25° horizontal grid spacing are adapted. Following Dinku et al. (2018), CHIRPS has been shown to feature a good relationship with station data over eastern EA at the monthly time-scale, outperforming other satellite-based products such as Tropical Applications of Meteorology using SATellite and ground-based observations (TAMSAT) and African Rainfall Climatology version 2 (ARC2). Observed SSTs are obtained from version 5 of Extended Reconstructed SST (ERSSTv5; Huang et al., 2017) at a 2° × 2° resolution. For additional validation, we evaluate the seasonal climatologies of atmospheric circulation from SEAS5.1 against the fifth generation of European Re-Analysis (ERA5; Hersbach et al., 2020) dataset, at a horizontal (vertical) grid spacing of 0.25° × 0.25° (37 pressure levels from 1000 to 1 hPa). ERA5 was chosen based on its demonstrated ability to represent SON extreme events and their associated dynamics and thermodynamics over East Africa (Gleixner et al., 2020; Cook and Vizy, 2021). The precipitation from the ERA5 reanalysis has been included in these figures in order to validate ERA5 with the CHIRPS reference. For consistency in comparison, both observed and reanalysis datasets are regridded to a 1° × 1° horizontal resolution based on linear interpolation and to seven pressure levels (1000, 925, 850, 700, 500, 400, and 300 hPa).

2.2. Methods

The model's Potential Predictability (PP) is estimated as the ratio between external (σ_{Ext}) and internal variance (σ_{Inte}), following the methodology of Rowell et al. (1995) and Kang and Shukla (2006). The external variance (also referred to as the signal variance) represents the variance of the ensemble mean anomalies, while internal variance (or noise variance) corresponds to the average variance of the deviations of individual ensemble members from the ensemble mean. These quantities are obtained through the following calculations:

$$\sigma_{Ext} = \frac{1}{N-1}\sum_{i=1}^{N}\left(P_i - \bar{P}\right)^2, \quad (1)$$

$$\sigma_{Inte} = \frac{1}{N(N-1)}\sum_{i=1}^{N}\sum_{j=1}^{n}\left(P_{ij} - P_i\right)^2, \quad (2)$$

$$P_i = \frac{1}{n}\sum_{j=1}^{n} P_{ij} \quad (3)$$

$$\bar{P} = \frac{1}{Nn}\sum_{i=1}^{N}\sum_{j=1}^{n} P_{ij} \quad (4)$$

$$PP = \frac{\sigma_{Ext}}{\sigma_{Inte}} \quad (5)$$

where P_{ij} is the model rainfall, P_i is the ensemble mean for the ith year and $\bar{P}$ the climatology mean of all data, with i = 1, 2, …., N (N= 43, the number of years) and j = 1, 2, …., n (n= 25, the ensemble size). All analyses were performed separately for each of the 25 ensemble members. The ensemble mean was then computed from the 25 members after applying all diagnostics to each individual member, including correlation and regression analyses, rainfall indices, composite anomalies, moisture flux, and moisture flux divergence, following the methodology of Abid et al. (2023).

This analysis uses two SST indices: the Niño 3.4 index (N34) and the Dipole Mode Index (DMI). The N34 index, used as a proxy for the ENSO, is defined as the area-averaged SST anomaly over the region 5° S–5° N, 170°–120° W (Trenberth, 1997). The DMI (Saji et al., 1999), which represents the IOD, is calculated as the difference between the area-averaged SST anomalies in the western Indian Ocean (WIO; 10° S–10° N, 50°–70° E) and the eastern Indian Ocean (EIO; 10°S-0° N, 90°–110° E).

To compute the composite anomalies, we subtract the 1981–2023 climatological mean from the composites of strong or weak events, for both the model forecasts and the observational data. To capture the variability of monthly rainfall over EA, the probability density function (PDF) based on the Gamma distribution, identified by Husak et al. (2006) as particularly appropriate for representing the asymmetric and limited nature of precipitation data, is employed. In this study, it is used to illustrate how the model, as well as the observations and reanalysis, represents the characteristics of both extreme and mean SON season rainfall over EA during the 1981–2023 period. This distribution can be expressed as follows:

$$f(P_i) = \frac{1}{\beta^{\alpha}\Gamma(\alpha)} P_i^{\alpha-1} e^{-P_i/\beta} for\ P_i > 0 \quad (6)$$

where α > 0 is the shape parameter, β > 0 is the scale parameter, P_i denotes the rainfall amount, and Γ(α) is the Gamma function.

Using the specific humidity (q) and horizontal wind vector (V) over the atmospheric column (1000-300 hPa), environmental conditions for extreme rainfall events are also analysed through an assessment of moisture flux convergence ∇·(qV). This quantity can be further decomposed into moisture convergence (q∇·V) and moisture advection (V·∇q), respectively, following the formulation presented by Cook and Vizy (2021) and Kolstad et al. (2024), as described by the following equation:

$$\langle \nabla \cdot (qV) \rangle = \langle q \nabla \cdot V \rangle + \langle V \cdot \nabla q \rangle \quad (7)$$

where V denotes the horizontal wind and q represents the specific humidity. The angle brackets "<>" signify the vertical integral from the surface (1000 hPa) to the top (300 hPa) of the atmosphere column.

Based on both CHIRPS and ERA5 dataset, extreme SON season rainfall over EA (8°-50° E; 10° S-10° N) were identified. The EA rainfall Index (EAI) is defined by averaging the observed SON rainfall anomalies over EA and normalising by their standard deviation. Strong (weak) years are defined as those in which the common CHIRPS and ERA5 EAIs exceed +0.5 standard deviation (fall below –0.5 standard deviation). Positive and negative composites analyses were then performed based on the years identified as strong and weak, respectively. Note that the same set of years was used for all observational, reanalysis, and model variables. For Pearson correlation/linear regression and composite anomaly analyses of rainfall and SST, statistical significance was determined using a standard two-tailed Student's t-test to estimate p-values. A 5% significance level was applied throughout, with results considered locally statistically significant if $p < 0.05$. It is important to note that the correction of p-values due to multiple testing was not addressed, in accordance with Wilks, (2016).

3. Model skills assessment

3.1. SEAS5.1 prediction of EA rainfall mean and variability

In this section, the model's ability to predict both monthly and SON season precipitation climatology is investigated. Figure 1 illustrates the annual precipitation cycle (Fig. 1a) and the precipitation fraction (Fig. 1b-d) from the CHIRPS dataset and the two lead-times (L0 or L1) of SEAS5.1. For this analysis, L0 and L1 correspond to the specific month and the month before, respectively. This means that June has June and May as L0 and L1, respectively. Overall, the model captures the CHIRPS annual rainfall cycle reasonably well, with a slight wet bias (0.2 to 0.6 mm day^{-1}) throughout the year for September IC or 0-month lead-time (L0 hereafter), except in July, similar to findings by Attada et al. (2022) over India. For August IC or 1-month lead-time (L1 hereafter), the model shows a wet bias (0.5 to 1.5 mm day^{-1}) from January to March and July to September, and a dry bias (0.3 to 1 mm day^{-1}) during April to May and November to December. At L1, the model fails to reproduce the observed rainfall peaks during March–May (MAM) and September–December (SOND) periods, unlike L0, which simulates them well. Notably, CHIRPS as well as the model at L0 both indicate rainfall peaks in April and October, while at L1, the model incorrectly shifts these peaks to March and September, respectively. During SON, the highest observed precipitation fraction (Fig. 1b) occur over the eastern part of EA (45–50 %), mainly over south-eastern Ethiopia, eastern Kenya and Somalia, as well as over Gabon and southern Cameroon (40–45 %). Conversely, values drop below 20 % over Tanzania and northwest of Kenya (Fig. 1b). This is consistent with findings by Gudoshava et al. (2022a,b), who also showed strong (weak) rainfall contributions over southern Ethiopia, eastern Kenya and Somalia (Tanzania and northwestern Kenya). The precipitation fractions forecasted at L0 and L1 (Fig. 1c,d) align with the observed maximum percentages of total annual

precipitation occurring over eastern EA, though the model underestimates (overestimates) at L0 (L1). Over western EA, SEAS5.1 slightly overestimates (underestimates) the precipitation percentage over the CB (Gabon and Equatorial Guinea) at L0, while at L1, it significantly overestimates (underestimates) rainfall contribution over southern (northern) parts of EA.

These results are consistent with the SON rainfall bias shown in Fig. S1a,b. At L0, the model shows a positive rainfall bias of around 3 mm day^{-1} and negative rainfall bias of around -1 mm day^{-1} over the CB (Gabon and Equatorial Guinea). In contrast, a larger positive bias (4 mm day^{-1}) in the southern region and a substantial negative bias (–4 mm day^{-1}) in the north are observed at L1. These findings indicate that SEAS5.1 performs better in simulating SON rainfall climatology over eastern EA, where both simulated error and absolute bias are less than 1 mm day^{-1} at both lead-times (Fig. S1) compared to western EA. Furthermore, performance is generally better at L0 (bias and error around 1 mm day^{-1}) than at L1 (around 4 mm day^{-1}).

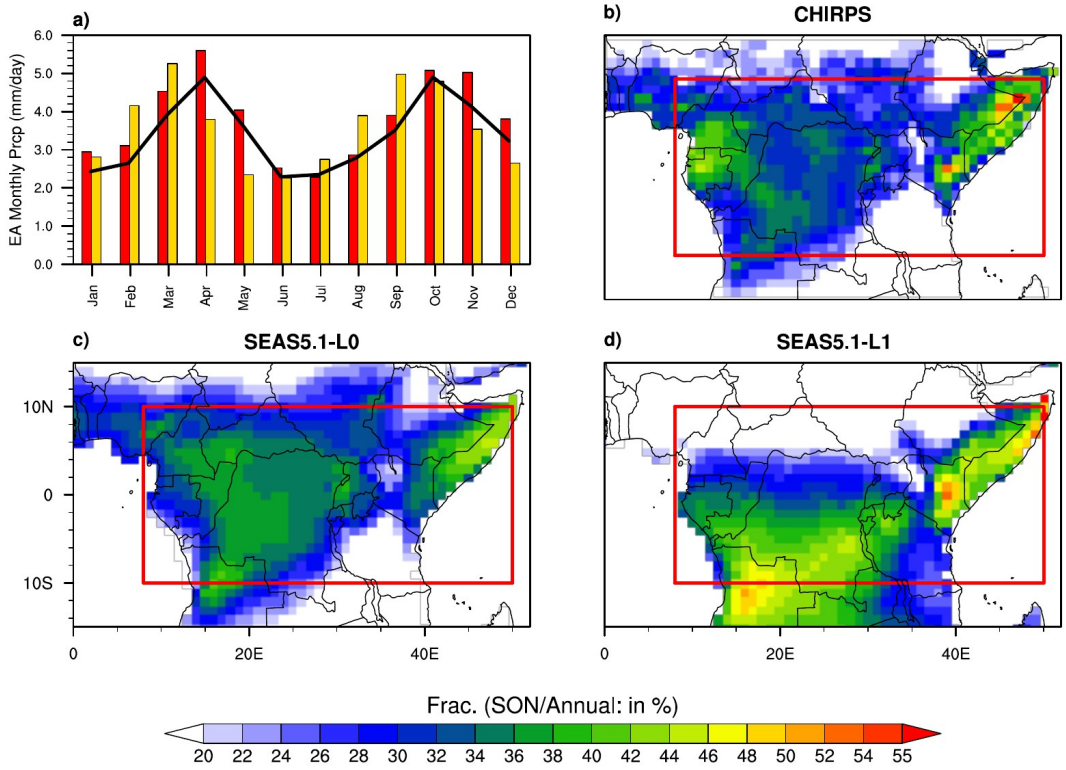

Fig 1: a) EA rainfall annual cycle comparing CHIRPS observation (black line) and SEAS5.1 over the period 1981-2023. The red (gold) bar indicates the L0 (L1) of the 25 ensemble members. Precipitation fraction [EA (SON/Annual, in %] for b) observation, c) 0-month lead (L0) model, and d) 1-month lead (L1) model. The red boxes in b), c) and d) indicate the EA boundaries.

In addition to the forecast skill assessment, the spatial distribution of the linear correlation coefficient (CC) between observed and simulated precipitation is shown in Fig. 2a,b to evaluate the ability of SEAS5.1 to simulate SON rainfall over EA (Nana et al.,

2024). The CC value varies between - 1 and 1, where values near 0 means no predictive skill, and values approaching 1 indicate good skill. At both lead-times, a large portion of EA features strong significant and positive correlations, except over the CB, Central African Republic (CAR) and southern Cameroon. These areas with positive and significant (low and non-significant) correlation values coincide with areas where the model bias and RMSE values are low and even null (strong). Overall, the model demonstrates better skill at L0 than at L1 across the region, consistent with the conclusions of Tefera et al. (2025). To further investigate the relationship between observed and predicted EA precipitation, Fig. 2c,d shows the scatter plot between CHIRPS and SEAS5.1 EA rainfall at L0 (Fig. 2c) and L1 (Fig. 2d). The red lines indicate the prediction interval (PI), while green lines indicate the confidence interval (CI). At L0, the data points, as well as the PI and CI are closer to the regression line, reflecting the strong relationship shown in Fig. 2a and the low simulated errors. Notably, the CI clearly widens as precipitation values deviate from the CHIRPS mean, indicating increasing uncertainty in the true mean as we move away from the CHIRPS mean. The PI also widens, but much more than the CI for any CHIRPS value. In contrast, at L1 (Fig. 2d), the data points are more dispersed, and both the PI and CI are further away from the regression line, which is also somewhat flatter than in at L0. This finding is consistent with the low CC values observed in Fig. 2b. Similar results were reported by Ehsan et al. (2021), who also shows that the CI (linear regression line) between June-to-September Ethiopian and SEAS5 precipitation moves away from the linear regression line (bit flat) as lead-time increases.

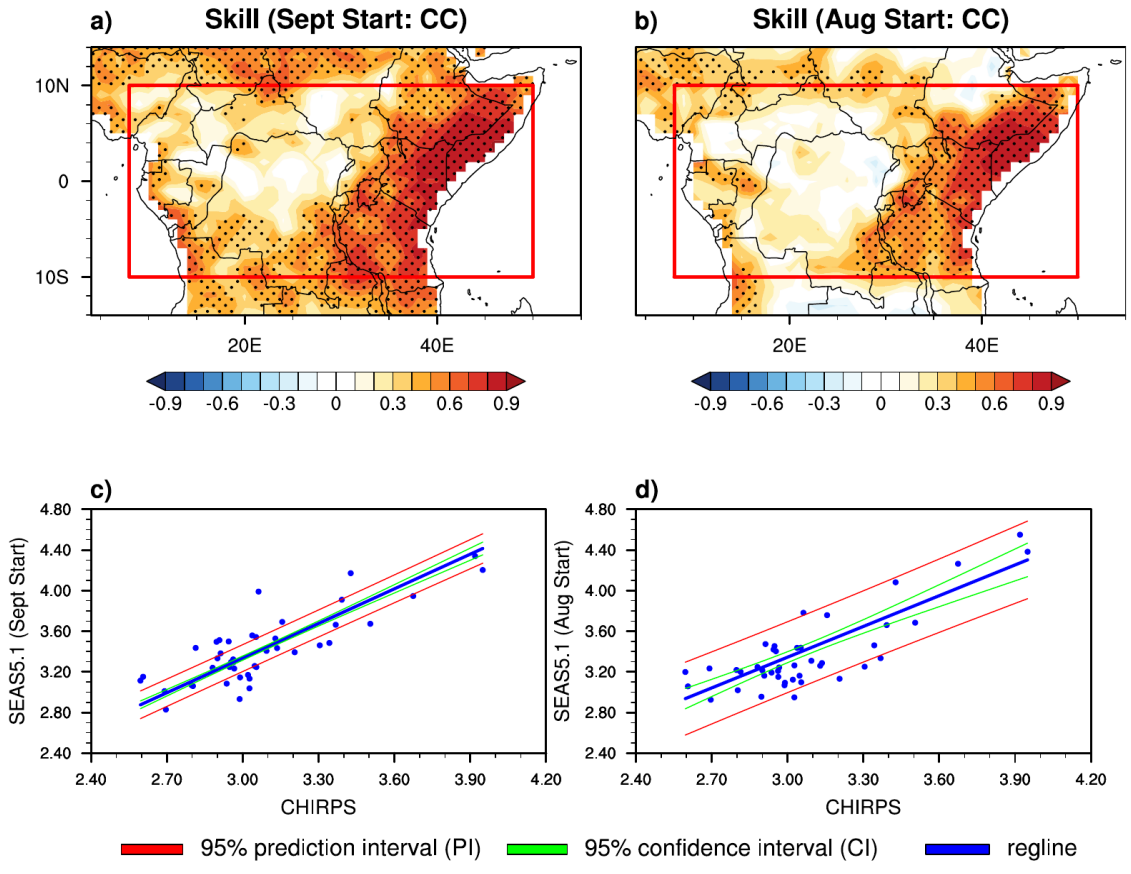

Fig 2: Spatial distribution of correlation coefficient (CC) between observation and ensemble mean precipitation data initialised in a) September, and b) August respectively. The stippling occurs where the correlation coefficient is locally statistically significant at 95% confidence level through the Student's t test. Joint plot (scatter plot) between observed (CHIRPS) and predicted (SEAS5.1) EA rainfall for c) September and d) August starts for 1981-2023. Blue line is the linear regression line, red (green) lines indicate the 95% prediction (confidence) interval of the model. The red boxes in a) and b) indicate the EA boundaries.

The spatial distribution of both external (first row) and internal (second row) variances along with the ratio (third row) of these two quantities, at L0 and L1 is represented in Fig. 3. The maximum external variance values (Fig. 3a,b) occur over western and eastern parts of EA at L0, with values around 1.5 mm^2 day^{-2} over eastern Kenya and Somalia. However, at L1, we observe a decrease in external variance, mainly over western EA, where many areas (Cameroon and Gabon) exhibit values less than 0.2 mm^2 day^{-2}. For the internal variance (Fig. 3c,d), the highest values occur at L1, and focus over Gabon, northern Angola, western Kenya and southern Tanzania. Then, the PP, as the ratio between external and internal variances is strong over coastal regions, higher at L0 (Fig. 3e) compared to L1 (Fig. 3f). These maximum values (around 3.8 at L0 and 1.3 at L1) occur where external variance outweighs the internal variance. It is noteworthy that these high values are obtained over the tropical oceanic region (Eastern and south-western EA) where precipitation is strongly modulated by the tropical SST, in line with the findings of Kang and Shukla (2006). These analyses show that the model performs well in simulating precipitation over the region, mainly over East Africa, Gabon and the western Republic of Congo. This performance is better at L0 than at L1 (Tefera et al., 2025). However, although the model performs well in forecasting precipitation over the region during the first two lead-times, it is important to assess its ability to predict the relationship between this precipitation and its main drivers, the SSTs over the Indian and Pacific Oceans (Moihamette et al., 2022; Roy and Troccoli 2024). The following section concerns the ability of SEAS5.1 to represent the observed teleconnection.

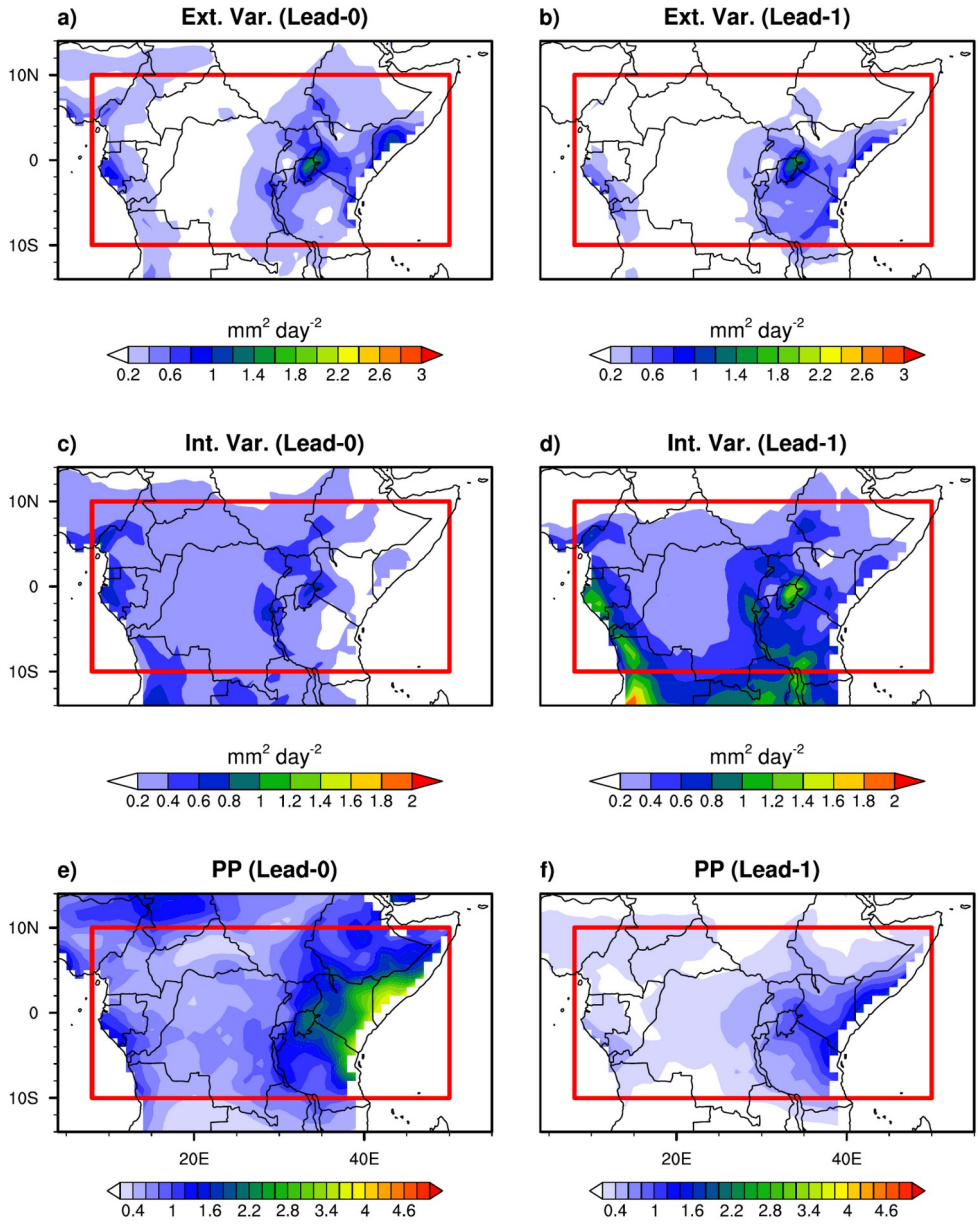

441

442 **Fig 3:** (a-b) External, (c-d) internal variances, and (e-f) PP for SON EA rainfall, for (first column) L0,
443 and (second column) L1 respectively. The red boxes indicate the EA boundaries.

444

445 ### 3.2. Physical mechanism and teleconnection patterns

446 Figure 4 shows the observed and simulated relationship through the regression
447 analysis, between EA rainfall and the DMI. The results highlight a predominantly
448 strong, positive and statistically significant regression between DMI and observed
449 rainfall over the eastern part of EA (east of 30° E; Fig. 4a). Over western EA, some areas
450 such as southern and northern DRC, and northern Angola also feature significant
451 positive regression values. However, other regions exhibit weak (both positive and

negative) and even zero regression values. These findings suggest that anomalously strong rainfall over EA is generally associated with positive IOD events, characterised by warming (cooling) of SST features over the western (eastern) pole of IOD, as mentioned by Nana et al. (2025); Roy and Troccoli (2024) and Tefera et al. (2025). Conversely, an opposing rainfall pattern is observed during negative IOD episodes. The regression pattern between the predicted DMI and EA precipitation at L0 (Fig. 4b) and L1 (Fig. 4c) is quite similar to that observed. However, it is noteworthy that at L0, the model tends to underestimate (overestimated) the IOD teleconnection over eastern (western) EA regions, mainly Ethiopian (DRC and southern Cameroon) regression values. At L1, the positive relationship over eastern EA shifted southwards, with highest values over Tanzania and southern Kenya, where observed regression values were lower. This analysis suggests that the IOD-EA rainfall relationship is well captured in the model, which aligns with the findings of Nana et al. (2024), who point out that ECMWF is the best forecast model (among eleven predicting models) that captures SST-rainfall relationship over EA.

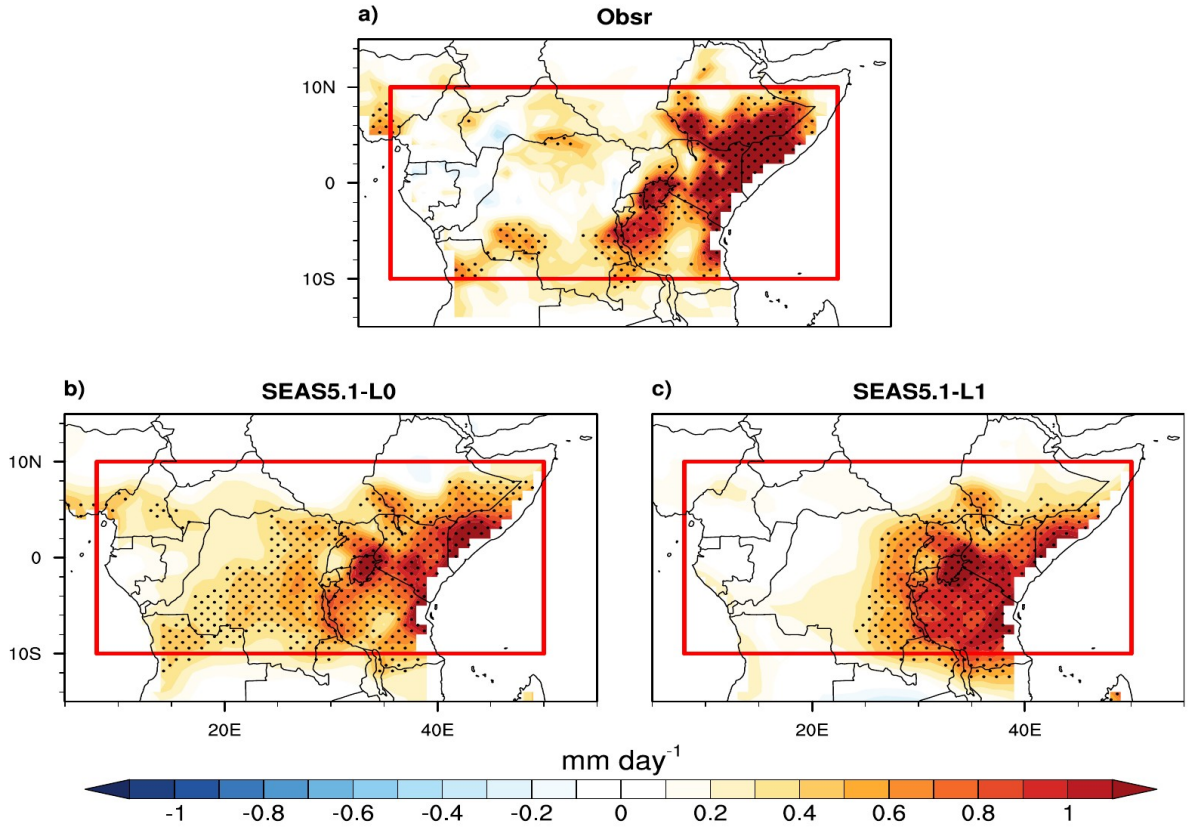

Fig 4: a) Regression of the standardised DMI with the Precipitation during SON; (b) and (c) same as of (a) but for the SEAS5.1 dataset at L0 and L1, respectively. Stippling denotes where the regression is locally statistically significant at 95% confidence level. The red boxes indicate the EA boundaries.

Furthermore, this regression pattern between DMI and EA rainfall remains consistent when an ENSO-type signal is present over the N34 region (Fig. 5). The results support the presence of IOD-like patterns over the IO and ENSO-like patterns over the equatorial Pacific, both in observation (Fig. 5a) and model (Fig. 5b,c). Both observation and model exhibit significant positive (negative) regression values over WIO (EIO). The equatorial Pacific highlighted here by the N3.4 index shows strong and significant positive regression (Tefera et al., 2025), suggesting that ENSO and IOD may exert over the region a concurrent influence on rainfall distribution. This suggests that ENSO can modulate or amplify the IOD signal when both phenomena occur simultaneously. Another noteworthy pattern emerges over the eastern equatorial Atlantic, where strong positive and significant regression values are observed (Fig. 5a). A recent study by Moihamette et al. (2024) shows that rainfall variability over the areas along the Atlantic coast during IOD events can be influenced by Atlantic SST anomalies through atmospheric bridge mechanisms. The model at both L0 and L1 successfully captures this Atlantic teleconnection. The model at both L0 and L1 appears to successfully capture this Atlantic teleconnection.

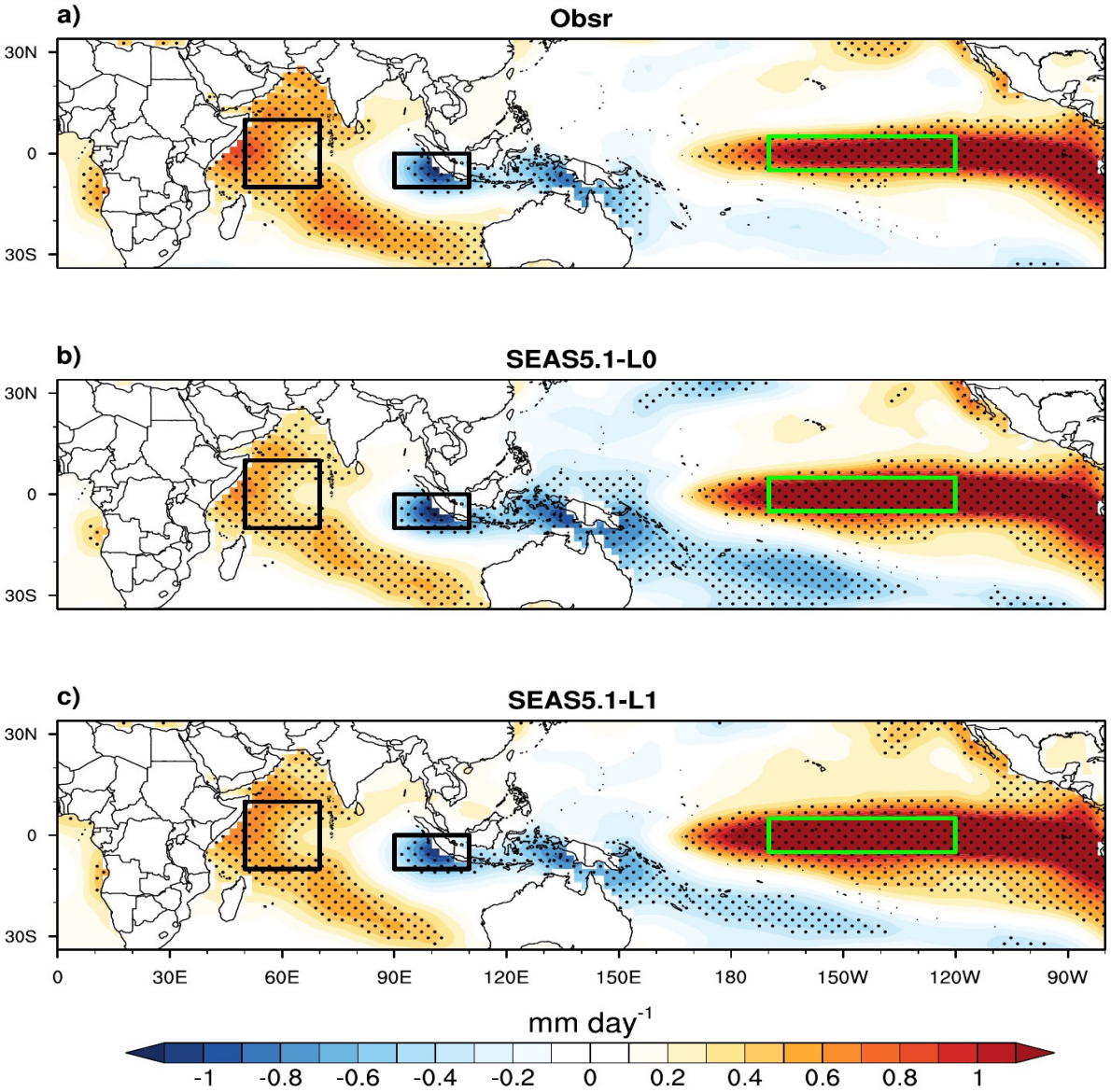

Fig 5: Same as Fig. 4, but for regression of the standardised EA precipitation with the global SST. The black and green boxes indicate the IOD and N34 oceanic regions, respectively.

To further analyse the relationship between EA rainfall and both ENSO and IOD, Figure 6a outlines the scatterplots of the observed EA rainfall with the IOD and N34 indices during the SON season. The relationship between the EA rainfall index and the DMI (black triangles) as well as N34 index (red circles) is clearly positive and statistically significant (at 95% confidence level) with correlations of 0.74 and 0.40, respectively. This confirms that IOD could have an impact on the EA rainfall independently of ENSO. Moreover, these outcomes suggest that ENSO has an indirect effect through IOD conditions, but also a direct impact on EA precipitation through an atmospheric bridge (Ibebuchi 2021; Roy and Troccoli 2024). The SEAS5.1 captures these relationships

reasonably well at both L0 and L1, but overestimated the correlations, mainly the ENSO-EA precipitation relationship (Fig. 6b,c).

Following the assessment of SEAS5.1 in simulating rainfall characteristics and their associated teleconnections with SST, the analysis is extended to a composite-based approach. This complementary framework allows a more detailed examination of the large-scale atmospheric and oceanic patterns associated with extreme rainfall events over EA. In particular, composites of precipitation, SST, and low-level wind fields are used to characterise the dominant circulation features and moisture transport pathways linked to these extremes. This approach provides additional physical insight into the mechanisms driving extreme rainfall beyond the skill-based evaluation of the model.

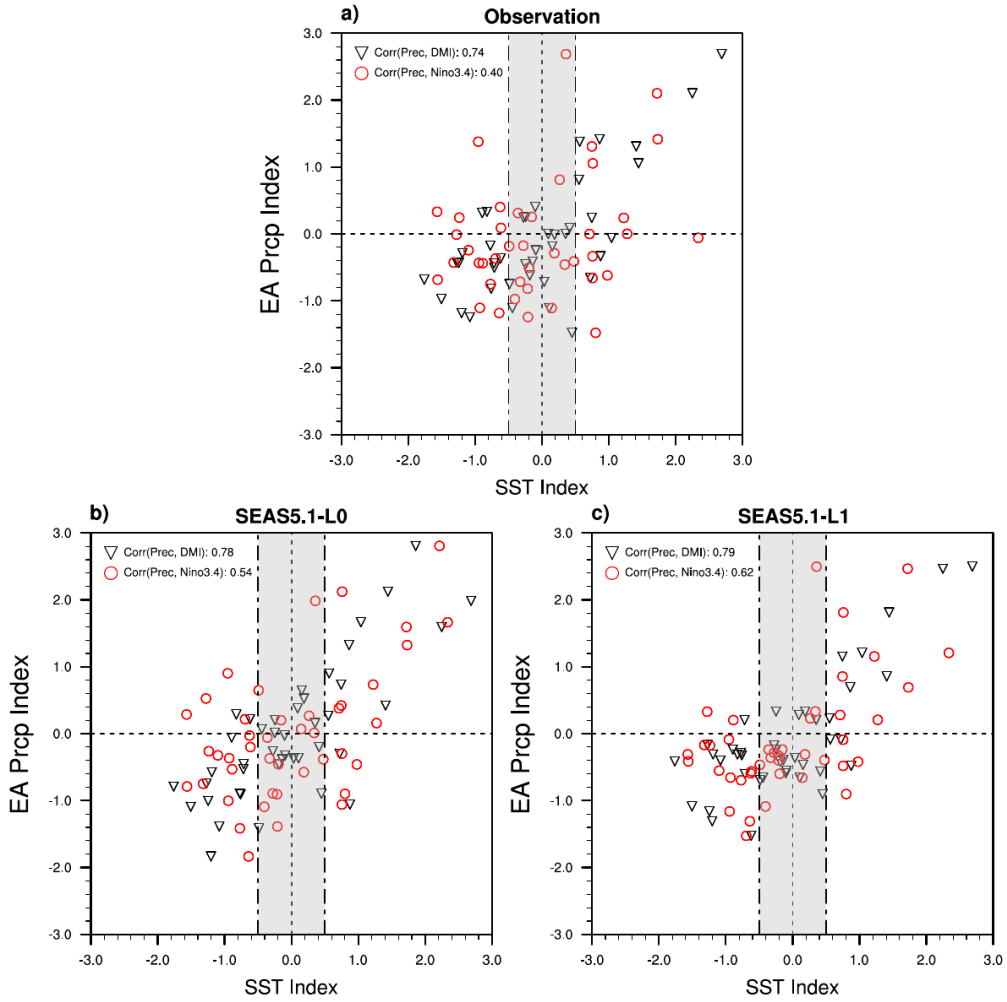

Fig 6: a) Observed Scatter plots for the EA precipitation with the DMI (black triangles) and N34 (red open circles) and SST based indices for the SON season. Note that the data points shown are ensemble mean values. The grey shaded region corresponds to ±0.5σ SST anomalies. Correlation Coefficient (CC) of EA precipitation index and DMI (N34) SST index is indicated at the top left of the map. (b) and (c) same as of panel (a) but for SEAS5.1 at L0 and L1, respectively.

4. Extreme EA rainfall: composites analysis

Firstly, we computed the time series of indices of standardised EA rainfall anomalies over the period 1981-2023 during SON season, for CHIRPS (red bar), ERA5 (blue bar), and SEAS5.1 at L0 (gold bar) and L1 (green bar). The CC between CHIRPS and SEAS5.1 EA rainfall index at L0 and L1 is 0.84 and 0.82, respectively (statistically significant at the 99% confidence level). Using the criteria described in Sect. 2.2 to detect extreme rainfall, years with strong and weak rainfall over EA are defined. Thirteen extreme rainfall years have been highlighted (Fig. 7), including seven Strong Years (SY) and six Weak Years (WY). Table 1 summarises the different extreme rainfall years based on both CHIRPS and ERA5 rainfall. Six (Five) of observed SY (WY) are captured by the model at L0, whereas six (two) are captured at L1.

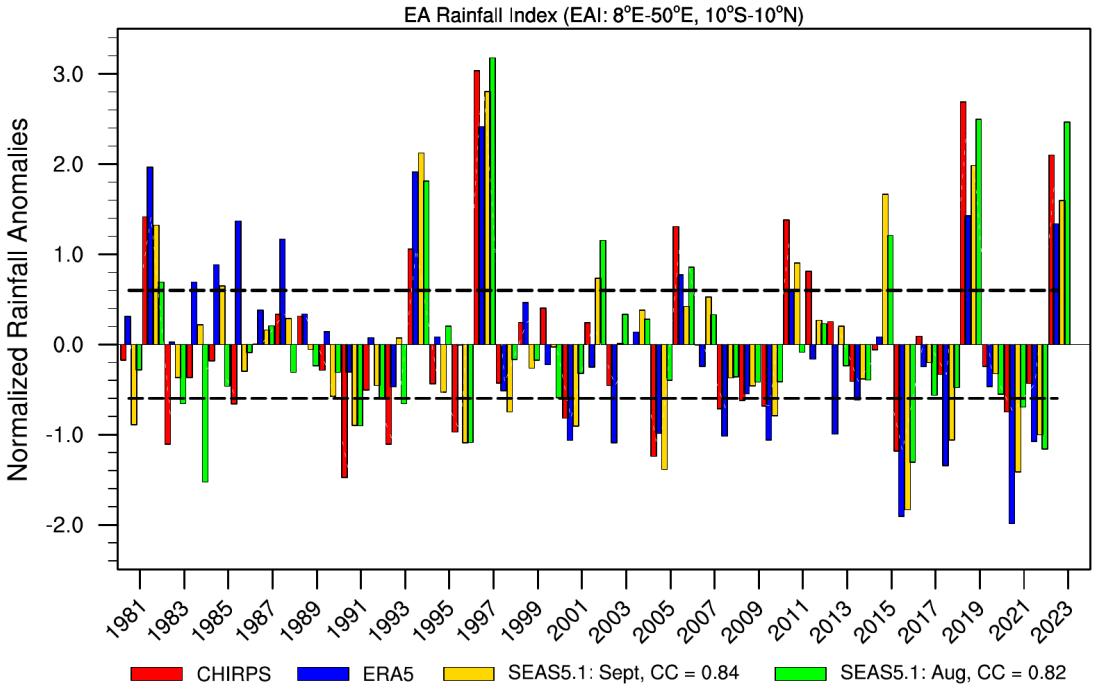

Fig 7: Indices of standardised EA rainfall anomalies over the period 1981-2023 during SON, for CHIRPS (red), ERA5 (blue), model at L0 (gold) and L1 (green). Dashed black line denotes ± 1 standard deviation of seasonal anomalies. The CC value between observed and predicted EA rainfall is shown in the legend below the map.

Table 1: Strong and weak EA rainfall years used in this study

Category	Years
Strong Years (SY)	1982*⊠, 1994*⊠, 1997*⊠, 2006⊠, 2011*, 2019*⊠, 2023*⊠
Weak Years (WY)	2001*, 2005*, 2008, 2010*, 2016*⊠, 2021*⊠

The asterisk (*) indicates the years captured by the model at L0, and the square (⊠) those captured by the model at L1.

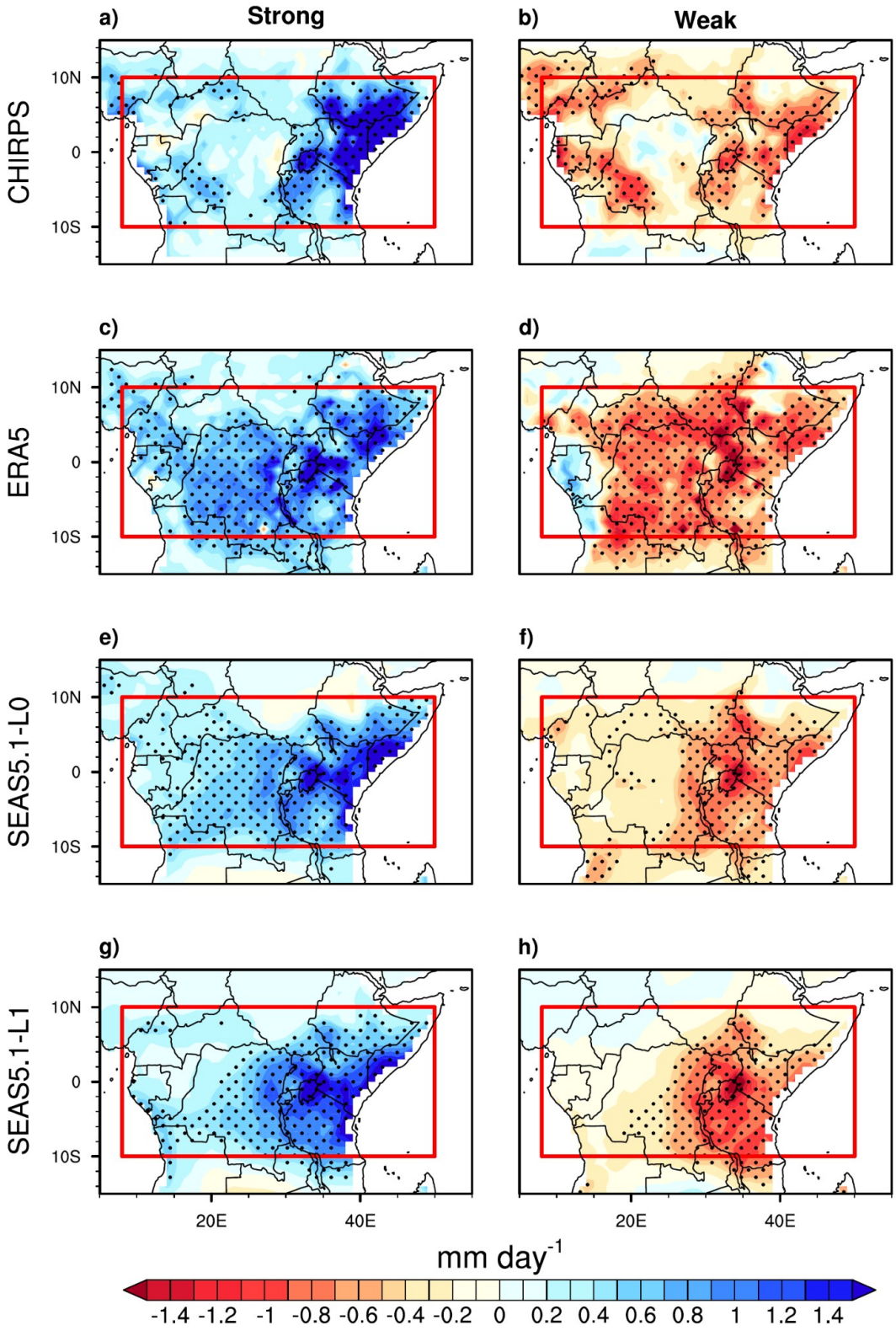

538

539 **Fig 8:** Composite of precipitation anomalies (in mm day^{-1}) during (first column) strong years and
540 (second column) weak years from (a-b) CHIRPS, (c-d) ERA5 and SEAS5.1 [L0 (e-f) and L1 (g-h)].
541 The red boxes indicate the EA region. The stippling occurs where the difference between the

composite and the mean climatology is locally statistically significant at the 95% confidence level through the Student's t test

Figure 8 shows the composites of EA rainfall anomalies for SY (first column) and WY (second column). It appears that during the observed SY composites (Fig. 8a,c), eastern EA experienced significant positive rainfall anomalies, mainly over southern Ethiopia and Somalia, as well as northern Kenya and Tanzania, where the IOD-rainfall relationship was strongest (Fig. 4a). Over the western EA, the positive rainfall anomalies are lower than over eastern EA, but are significant over certain areas (southwest of DRC and eastern CAR), where the IOD-rainfall relationship was strongest also. An opposite pattern is observed during the observed WY composites (Fig. 8b,d), but with a weaker (stronger) anomalies magnitude over the eastern (western) part of the EA, especially over Ethiopia, Kenya and Somalia (Cameroon, Gabon and DRC). It is important to note that ERA5 poorly represents precipitation anomaly values over the central part of the domain, particularly over the DRC, compared to the CHIRPS reference. This is explained by ERA5's low skill in these regions (Fig. S2). These observed characteristics of the rainfall composites are well simulated by the model at L0 (Fig. 8e,f) as well as at L1 (Fig. 8g,f), but with a lower magnitude compared to observations (mainly during WY composites; Fig. 8f,h). During the SY composite at L1 (Fig. 8g), the northern (southern) rainfall anomalies of eastern EA are underestimated (overestimated), a similar pattern with the positive IOD-rainfall relationship over eastern EA which shifted southwards at this Lead-time (Fig. 4c).

The monthly precipitation PDFs over EA during climatology mean (black line) SY (blue line) and WY (red line) are further investigated using gamma distribution (Fig. S3). The results confirm that more (less) observed/reanalysis rainfall are occurring over EA region during SY (WY) composites, compared to the SON mean climatology (Fig. S3a,b). These PDFs patterns were predicted successfully by SEAS5.1 at L0 (Fig. S3c) as well as at L1 (Fig. S3d).

Previous studies highlighted the fact that spatial pattern of extreme rainfall over EA is strongly influenced by SST anomalies in the surrounding ocean basins (Palmer et al., 2023; Roy et al., 2024; Nana et al., 2023,2025). Examining the associated SST composites therefore provides essential insight into the drivers of these rainfall extremes, and highlights the importance of accurately representing oceanic conditions in seasonal prediction models (Nana et al., 2024). To get an insight into the way SST responds to extreme rainfall events over EA, the composites of global SST anomalies for SY and WY events are presented in Fig. 9. As seen in Fig. 5, favourable conditions for the occurrence of EA rainfall is associated with warming (cooling) of the SST over WIO (EIO) areas (black boxes in Fig. 5), and warming of the SST over the ENSO region (green boxes in Fig. 5). It appears that during observed SY composites (Fig. 9a,c), the IO shows significant warming (cooling) of the SST located over WIO (EIO) while the area of interaction of Niño-3.4 simultaneously exhibits strong and positive SST anomalies,

583 characterising El Niño events. An opposite pattern is observed during the WY years
584 (Fig. 9b,d). It should be noted that the EIO exhibits stronger SST anomalies than those
585 over the WIO, suggesting that IOD intensity is strongly modulated by the SST changes
586 over the EIO, as suggested by Cai et al. (2011). It is important to note that SST anomaly
587 values are stronger during the SY composites compared to those observed during WY
588 events. This can be explained by the fact that, among the seven SY years, three
589 correspond to El Niño record events (1982, 1997, 2023) and two to moderate events
590 (1994 and 2006), with six of them also coinciding with positive IOD episodes. In
591 contrast, among the six WY years, only one corresponds to a significant La Niña event
592 (2016) with four moderate events (2005, 2008, 2010, 2021), while four are associated
593 with moderate negative IOD episodes. These outcomes confirm that the anomalous
594 extreme rainfall which occurs over EA during the SON season are strongly associated
595 with SST anomalies over these two oceanic regions. The above results and conclusion
596 are in agreement with recent findings by Nana et al. (2025). The model predicted these
597 observed composite patterns well at L0 (Fig. 9e,f) and L1 (Fig. 9g,h). The observed SST
598 anomalies, as well as rainfall anomalies (Fig. 8) stronger during SY than during WY, are
599 well simulated by the model at these two Lead-time. During SY events, for both
600 initialization conditions, the model successfully captures the spatial distribution and
601 intensity of SST anomalies (Fig. 9e,g), which is consistent with its good performance in
602 reproducing the associated rainfall anomalies (Fig. 8e,g). In contrast, during WY events,
603 the model overestimates SST anomaly amplitudes across the three domains (Fig. 9f,h),
604 with the largest biases occurring in the western IOD box. This warm bias likely
605 contributes to more rainfall anomalies simulated by the model (Fig. 8f,h) compared to
606 observation (Fig. 8b). This finding is in line with Moihamette et al. (2024), who
607 demonstrated that the western IOD pole plays a dominant role in the IOD-precipitation
608 relationship over the region during the SON season.

609

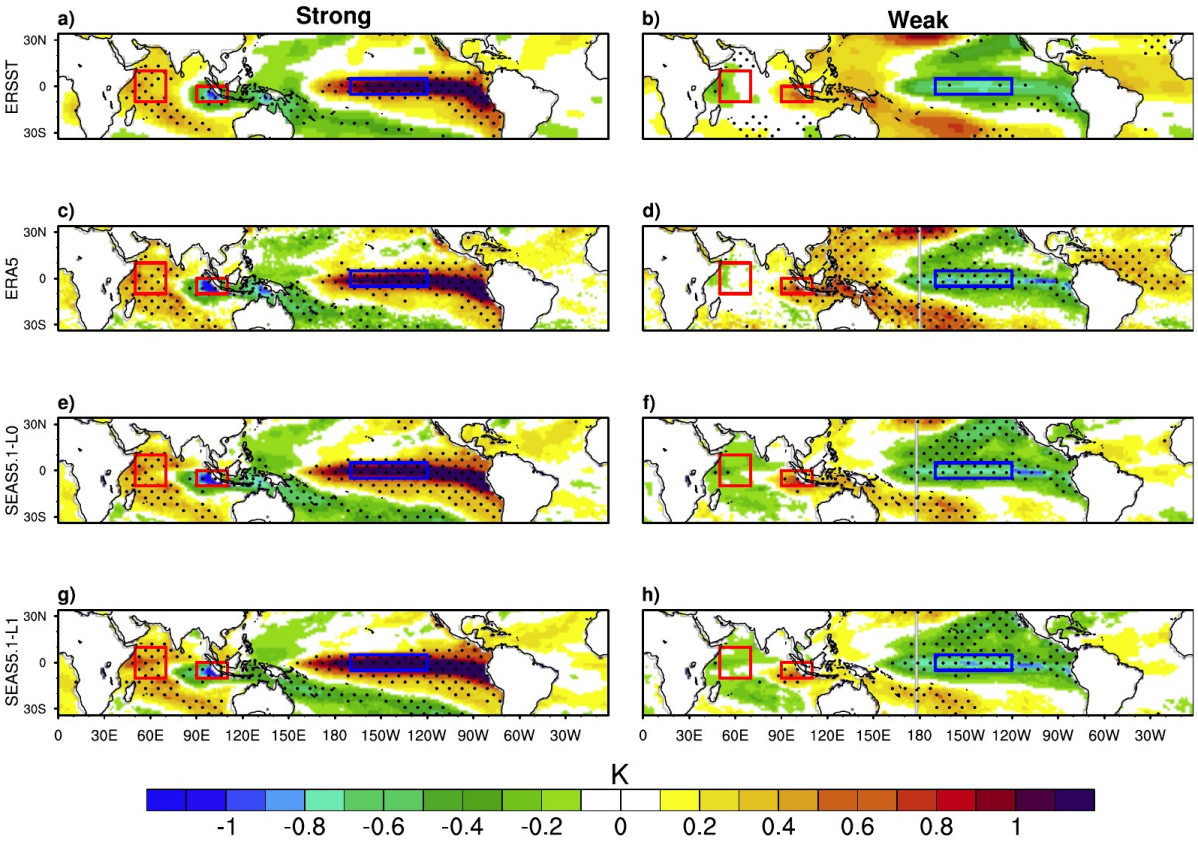

Fig 9: Same as in Fig. 8, but for SST (in K). The red and blue boxes indicate the IOD and N34 oceanic regions, respectively.

5. Atmospheric circulation: composites analysis

Previously, observed and reanalysis, as well as predicted composite SST anomalies over the Atlantic, Indian, and Pacific oceans showed a strong and significant composite anomalies pattern during both strong and weak years (but more pronounced during SY than WY), which shows that EA rainfall has diverse dynamical linkages from these oceanic regions. We are now interested in the large-scale control of EA precipitation, as, following Nana et al. (2023, 2025) and Dezfuli and Nicholson (2013), interannual variations in EA precipitation are strongly influenced by large-scale climatic factors such as east Atlantic SST, IOD and ENSO. Figure 10 investigated the model's ability to predict large-scale circulation patterns through horizontal wind at 850 hPa and MSLP. During SY (WY) composites, the eastern and western equatorial IO experience strong easterly (westerly) wind anomalies, while eastern equatorial Atlantic exhibits weak westerly wind anomalies (Fig. 10a,b). According to Moihamette et al. (2024) and Nana et al. (2025), strong (weak) circulation patterns over the EA region are predominant during excess (deficit) rainfall years as a result of large-scale circulations from both equatorial Indian and eastern Atlantic oceans. These circulation patterns are associated with dipole mode over IO, more pronounced during SY (Fig. 10a) than WY (Fig. 10b), characterised by strong positive (negative) and significant values over EIO

(WIO). Also, the southeast Atlantic coastal region exhibits negative composite anomalies (Fig. 10a). This is consistent with the work of Dezfuli and Nicholson (2013), who found that SY (WY) events over eastern EA are associated with negative (positive) MSLP anomalies over WIO (EIO), whereas negative (positive) MSLP anomalies over southeast Atlantic coast occur during SY (WY) events over western EA. These observed composite features are well predicted with the September IC (Fig. 10c,d) and August initial condition predictions (Fig. 10e,f). The MSLP anomalies are underestimated by the model during SY (WY) at L0 (L1), mainly over WIO (whole of the EA as well as oceanic areas). These changes in SST (Fig. 9), wind and MSLP (Fig. 10) during the two rainfall events appear to be contrasted mainly over Indian ocean (strongly over the equatorial IO) compared to the equatorial Atlantic, and according to Nicholson (2015) and Nana et al. (2025), are responsible for the moisture supply over the EA during SON season.

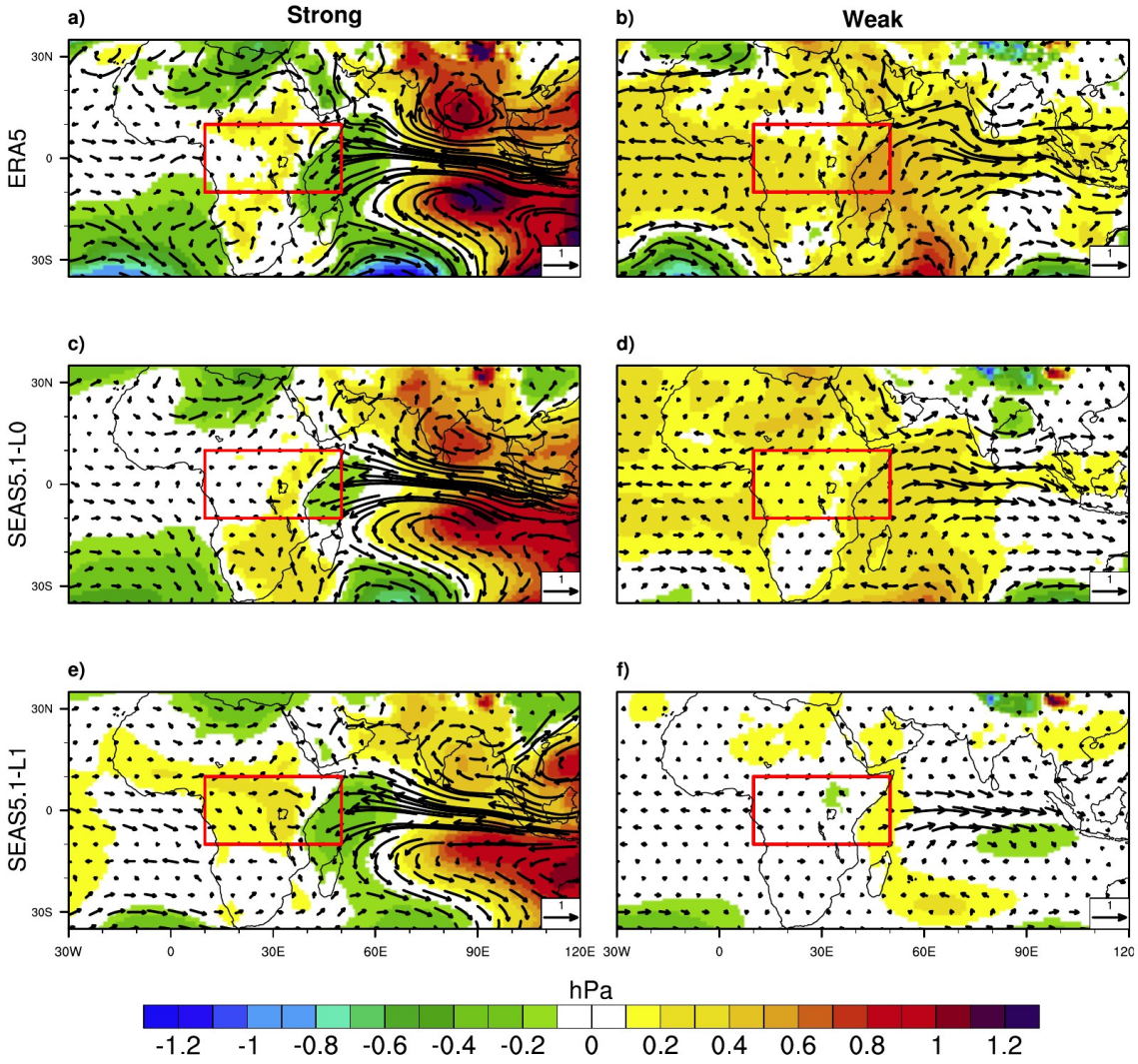

Fig 10: Same as in Fig. 8, but for MSLP (shading, in hPa) and 850 hPa wind (vector, m s^{-1}). The value higher (lower) than 0.02 (-0.02) hPa is locally statistically significant at 95% confidence level

To highlight the atmospheric layer responsible for the moisture surplus or deficit over the region during the two extreme EA rainfall, we have examined in Figure 11 the vertical profile of the longitude-height cross-section of the observed and predicted zonal moisture flux between 1000-300 hPa, overlaid by the zonal wind and averaged between 10° S-10° N. The first column shows the SON mean climatology, the second and third column show the strong and weak composite anomalies, respectively. It emerges that the model successfully predicted the observed westerly climatology moisture transport (first column) as well as westerly wind from Atlantic Ocean to western EA in the lower troposphere (1000-850 hPa, around 0°-15° E). This observed and forecast configuration in the lower troposphere over the eastern Atlantic Ocean and western EA is the same as that observed 1000-550 hPa over the Indian Ocean. However, we note an underestimation of both moisture flux (shade in Fig. 11g) and wind at L1 (dash and solid lines in Fig. 11g). During SY (second column), anomalous easterly moisture transport occurs from IO (45° -90° E; in total troposphere) to EA (strong over middle troposphere in the eastern part), whereas the western part of EA exhibited strong westerly moisture transport in the middle troposphere (850-600 hPa) from the equatorial Atlantic ocean (Fig. 11b). In the lower troposphere (1000–850 hPa), easterly moisture transport prevailed over the EA region, whereas a westerly circulation appeared only in the mid-troposphere (850–600 hPa), with a weaker intensity compared to that originating from the IO. The easterly moisture transport anomalies over IO are well captured by the model (Fig. 11e,h). However, the model overestimated (underestimated) the easterly (westerly) moisture transport over east (west) of 13° E over the middle troposphere (850-600 hPa) at L0 (Fig. 11e), whereas an overestimation (underestimation) of westerly (easterly) moisture transport featured over western (eastern) EA over west (east) of 30° E between 1000-500 hPa at L1 (Fig. 11h). During WY (third column), observation (Fig. 11c) as well as model at L0 (Fig. 11f) and L1 (Fig. 11i) shows westerly (easterly) moisture transport over the Indian (Atlantic) ocean. Over western EA domain (between 13° E and 30° E), the model at L0 and L1 shows easterly moisture flux anomalies while observation shows westerly anomalies, but underestimated the observed Atlantic eastern moisture transport. In addition, anomalous westerly winds are weakened and easterly winds develop in the mid-troposphere (at 700 hPa), favouring equatorial easterly moisture transport. We can conclude that the two lead-time of the forecast model agree with two distinct mechanisms controlling moisture transport, over the ocean and the continent.

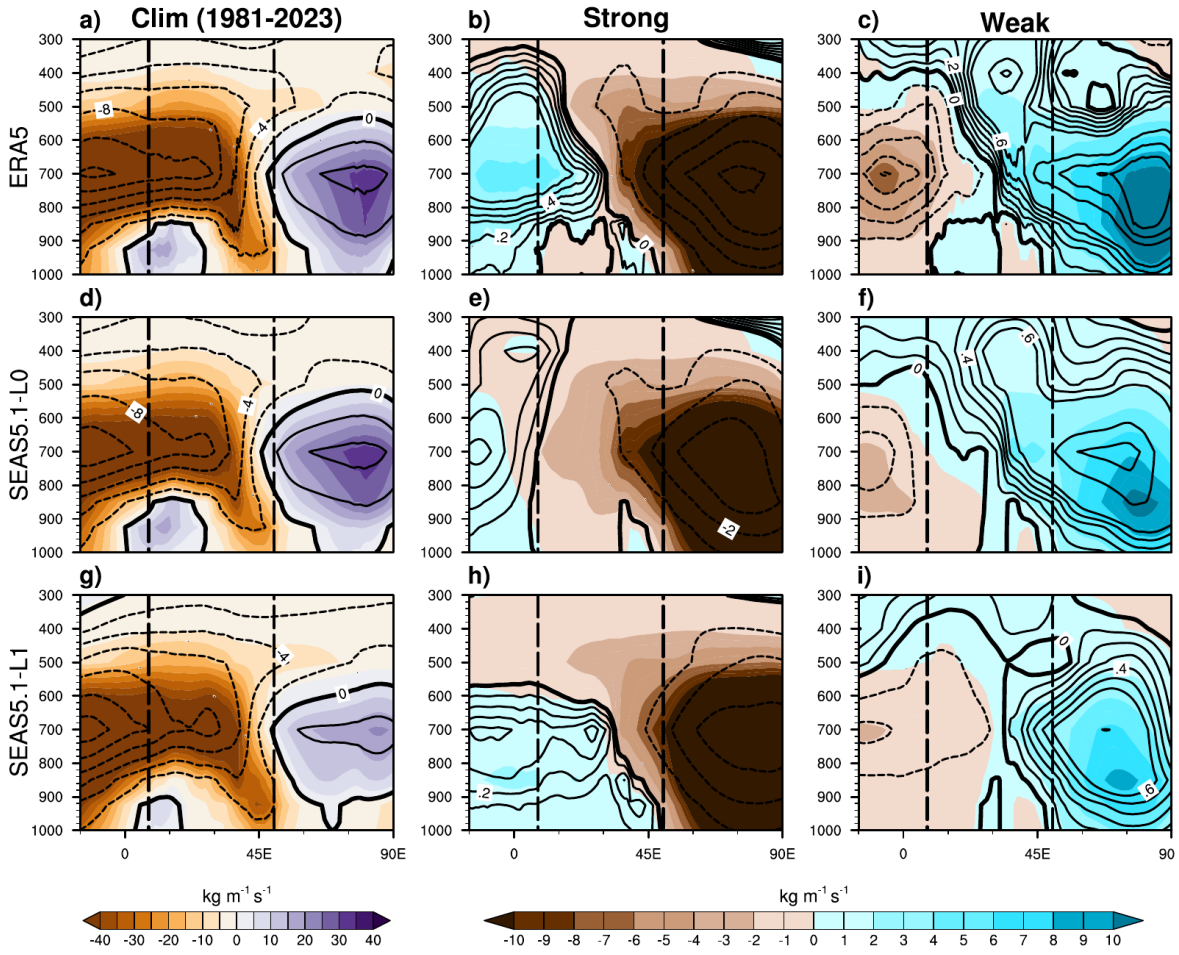

683

684 **Fig 11:** Longitude-height cross-sections for (first column) mean climatology of SON 1981-2023,
685 (second column) strong years composite anomalies and (third column) weak years composite
686 anomalies of zonal moisture flux (shading, kg m^{-1} s^{-1}) and zonal wind (contour, m s^{-1}) for (a-c)
687 ERA5, (d-f) L0 and (g-i) L1, averaged between 10° S-10° N. The dashed black lines denote the
688 limits of EA.

689

690 An important atmospheric feature over western East Africa is the African
691 Easterly Jet (AEJ), defined as the maximum easterly winds in the mid-troposphere (700–
692 600 hPa; Nicholson and Grist 2003). During the September–November rainfall season,
693 the AEJ shows a southern branch (AEJ-S) with its core near 10°S, and a northern branch
694 (AEJ-N), which occurs year-round with its core near 10°N (Kuete et al., 2022). The
695 following analysis highlights the characteristics of these features during extreme
696 September–November rainfall episodes.

697 The Figure 12 evaluated the column stratification of atmospheric convergence
698 through the latitude/height cross-sections of the net zonal moisture flux (shading)
699 calculated from West boundary (10° E) minus East boundary (30° E) boundary of
700 western EA over which the AEJ components (black dashed contours) at 15° E, and

specific humidity (red contours) calculated between 10°E and 30°, are overlaid. The first column shows the SON mean climatology of three tools, the second column shows the zonal moisture flux, AEJ and specific humidity composite anomaly for the SY composites, as well as the third column, but for the WY composites. The findings by Kuete et al. (2019) and Nicholson and Grist (2003) show that wet conditions over western EA are associated with decrease of the two AEJ components through increase in the middle tropospheric moisture convergence. Overall, the zonal net moisture flux balance over the EA shows a different structure for climatology and composites characterised by convergence in the middle troposphere (Fig. 12a-c) modulated by both southern and northern AEJ components, AEJ-S and AEJ-N respectively. During SY (Fig. 12b) composites, the AEJ-S and AEJ-N core speeds decrease compared to the climatology (Fig. 12a), leading to increase in moisture convergence over western EA (between 10° S and 10° N) favouring wet conditions over western EA, whereas the moisture divergence decreases at both 10° S and 10° N boundaries of EA favouring dry conditions, following Kuete et al. (2019) and Nicholson and Grist (2003). This middle tropospheric moisture convergence is accompanied by positive specific humidity anomalies. During WY (Fig. 12c) events, the two AEJ components are slightly stronger compared to the climatology, resulting in a strong divergence at 10° S and 10° N boundaries, and a weak mid-tropospheric convergence that contributes to intensified middle tropospheric divergence and followed by negative values of specific humidity anomalies. A similar pattern is observed at L0 (Fig. 12d-f), but slightly underestimated. In particular, the differences in the westward/eastward structure of the zonal moisture flux and associated wind anomalies appear to be dynamically consistent with the spatial distribution of forecast skill discussed in the previous section. At L1 (Fig. 12g–i), the southward displacement of the AEJ-N core (around 5°N instead of 10°N as in observations and L0) is associated with enhanced mid-tropospheric divergence and a reduction of the observed moisture convergence over western EA. In addition, the absence of the AEJ-S in both the climatology and composites suggests that the model fails to properly represent the meridional coupling between the two AEJ branches that modulates moisture convergence during SY and WY events. These circulation biases likely affect the zonal moisture transport between 10°E and 30°E, altering the westward/eastward extension of moisture flux anomalies. As a consequence, the model may misplace or weaken the mid-tropospheric convergence zone that is dynamically linked to wet conditions over western EA. This displacement and structural bias provide a plausible dynamical explanation for the reduced forecast skill identified in specific regions, particularly where the model underestimates moisture convergence anomalies.

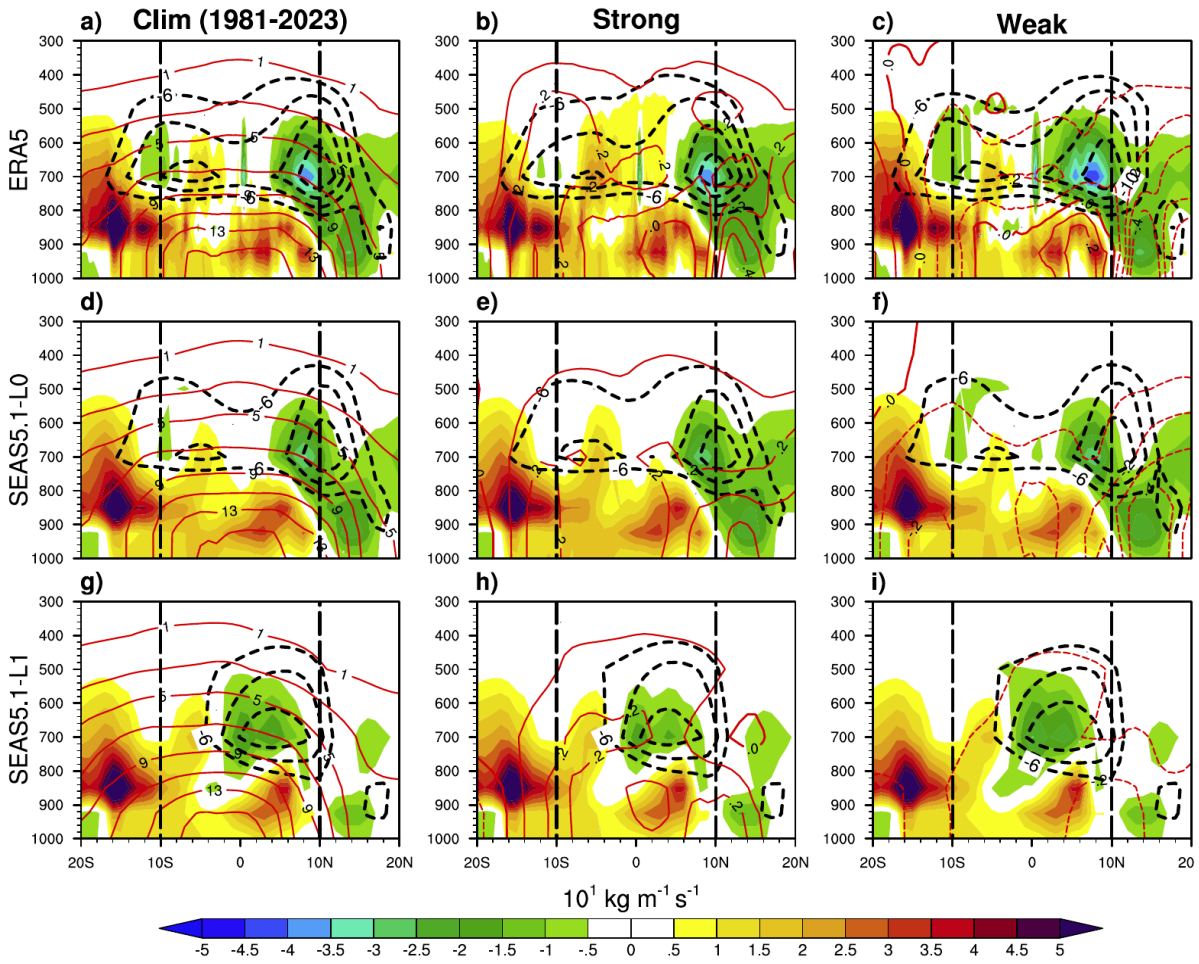

738

739 **Fig 12:** Latitude/height cross-sections of net zonal moisture flux (shading, 10^1 kg m^{-1} s^{-1})
740 calculated from West boundary (10° E) minus East boundary (30° E) for (first column)
741 climatology of SON 1981-2023 and (second column) strong years composite anomalies and
742 (third column) weak years composite anomalies. Black dashed lines represent AEJ components
743 (U<-6 m s^{-1}) with the contour interval 2 m s^{-1}, calculated at 15° E for the respective periods. Red
744 solid (dashed) lines represent SON mean climatology (composite anomalies) of specific humidity
745 with the contour interval (first column) 2 Kg Kg^{-1} and (second and third column) 0.1 Kg Kg^{-1},
746 averaged over 10°-30° E for the respective periods. Positive values indicate moisture flux
747 convergence, and negative values moisture flux divergence. The dashed black lines denote the
748 limits of EA.

749

750 The vertically integrated moisture flux divergence (VIMFD) and vertically
751 integrated moisture flux (VIMF) are important indicators of regions expected to receive
752 rainfall. To provide a further exploration of the ability of ECMWF-SEAS5.1 forecasts to
753 predict periods of heavy precipitation over the EA, we investigated the spatial patterns
754 of both observed (Fig. 13a,b) and predicted (Fig. 13c,f) VIMFD anomalies over 1000-300
755 hPa during SY and WY composites. SY (Fig. 13a) composite is characterised by an
756 anomalous VIMF associated with easterly and westerly flux over WIO and eastern
757 equatorial Atlantic, respectively. This moisture advection extends across the EA with

anomalous strong moisture convergence leading to wetter conditions over the region, with highest moisture convergence anomaly values occurring over the eastern EA. An opposite pattern feature during WY composite (Fig. 13b). Although underestimated, the observed pattern is well predicted by the model at L0 (Fig. 13c-d) and L1 (Fig. 13e-f). However, the model fails to simulate the westerly (easterly) flow over the Atlantic Ocean during the SY (WY) composites at L0, in contrast to L1 where these flows are represented, although underestimated by the model. Furthermore, examination of Figures S4 and S5 confirms that moisture convergence is the main component of moisture flux convergence, since, the spatial pattern of moisture convergence ($q\nabla\cdot V$) is similar (and with the same strengths) to that of moisture flux convergence ($\nabla\cdot(qV)$), in contrast to that of moisture advection ($V\cdot\nabla q$). This finding is in line with previous research by Longandjo and Rouault (2023) and Kolstad et al. (2024), who show that moisture convergence prevails in moisture flux convergence over western EA and eastern EA, respectively. The model captures this moisture convergence very well as the main component of moisture flux convergence (Kolstad et al., 2024) at L0 (Fig. S4c,d and Fig. S5c,d) and L1 (Fig. S4e,f and Fig. S5e,f). In summary, precipitation in the September and August IC predictions is reasonably represented, mainly driven by dynamic processes from the IO, supporting the use of SEAS5.1 outputs for eastern EA rainfall.

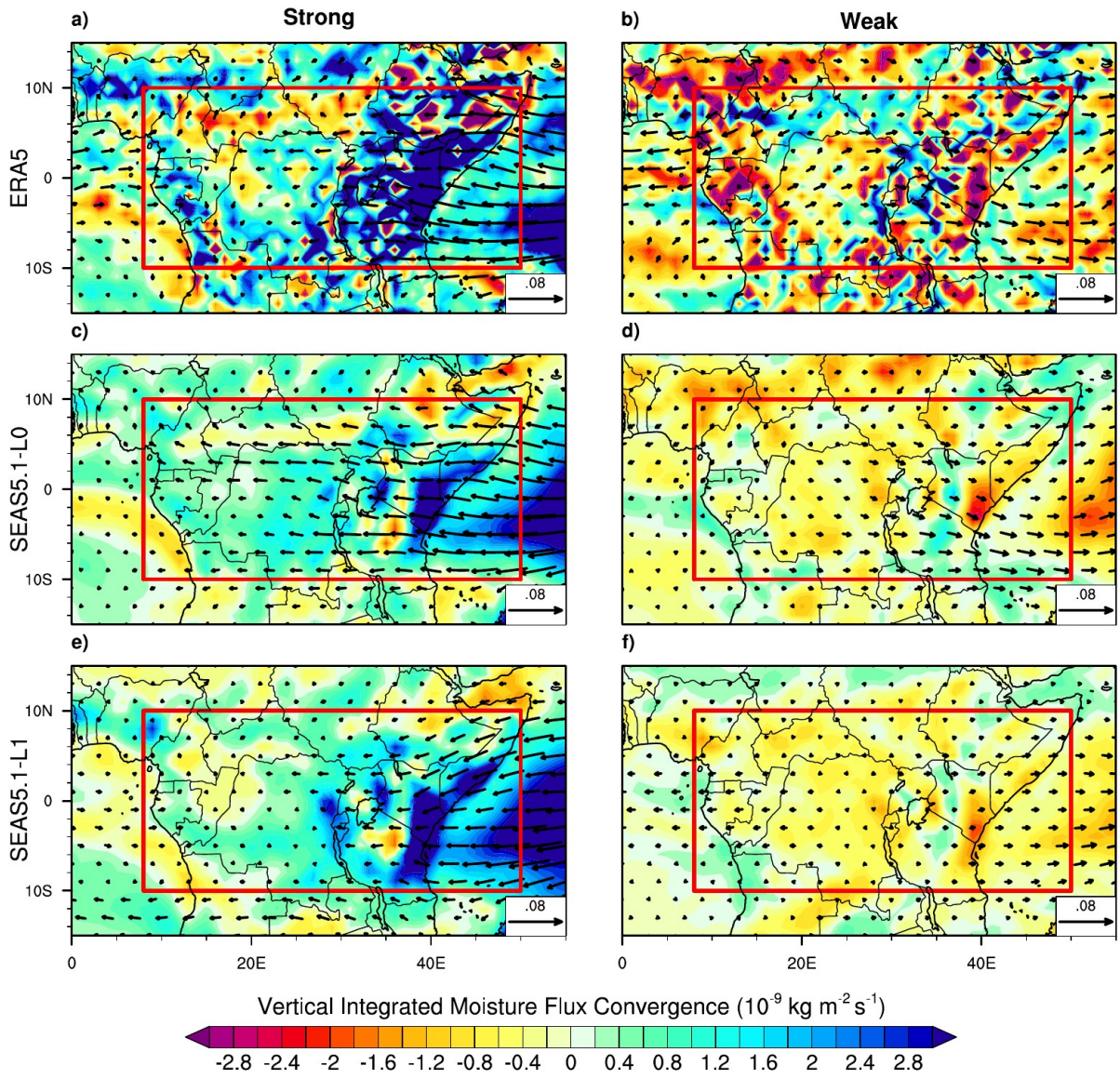

778

779 **Fig 13:** Same as Fig. 8, but for vertically integrated (1000-300 hPa) moisture flux (vectors, 10^{-9} kg
780 m^{-1} s^{-1}) and vertically integrated moisture flux convergence (positive values) or divergence
781 (negative values) anomalies (shading, 10^{-6} kg m^{-2} s^{-1}). Only locally significant vectors and shading
782 above the 90 % level are shown. The red box indicates the EA region.

783

784

785

786

787

788

6. Summary and conclusions

By analysing hindcasts and forecasts from the latest operational seasonal forecasting system based on dynamical climate models, the European Centre for Medium-Range Weather Forecasts seasonal prediction system 5, version 5.1 (ECMWF-SEAS5.1), this study highlights the influence of atmospheric drivers in forecasting extreme precipitation events over EA during the September–October–November (SON) season for the period 1981–2023. While some anomalous rainfall patterns over eastern and western EA have been linked to moisture transport from the Indian and Atlantic oceans respectively, further investigation is needed to evaluate the model's ability to simulate Madden–Julian Oscillation (MJO) activity during these extreme events.

The results indicate that the spatiotemporal and interannual variability of EA rainfall is generally well represented by ECMWF-SEAS5.1 in both lead-times during SON. However, the model exhibits limited skill in predicting rainfall over the Congo Basin, where hindcast data points are more dispersed at L0 than at L1, and both prediction and confidence intervals deviate more strongly from the regression line at L0. Predictability skill is higher for shorter lead-times (September IC), particularly over Kenya, southern Somalia, and northern Tanzania. Moreover, ECMWF-SEAS5.1 successfully reproduces large-scale teleconnections between tropical sea surface temperatures over the Atlantic, Indian, and Pacific oceans and precipitation over EA, with forecasts initialised in September (L0) showing stronger teleconnection skill than those initialised in August (L1). For September ICs, the model captures 85.71% of strong rainfall years and 83.3% of weak years, while for August ICs, it captures 85.71% of strong years and 33.3% of weak years.

The model also demonstrates its ability to reproduce maximum composite rainfall anomalies over eastern EA, particularly across Kenya, southern Ethiopia, and Somalia, although it tends to underestimate their magnitude. Both the Indian Ocean Dipole (IOD) and ENSO modes are realistically simulated during extreme events and for both lead-times, along with their associated atmospheric circulation. Furthermore, ECMWF-SEAS5.1 accurately simulates moisture flux convergence and its components (moisture convergence and moisture advection), with relatively stronger performance for September IC compared to August. Overall, the system shows strong and statistically significant skill in reproducing atmospheric features linked to extreme rainfall events over EA, with higher performance in the eastern sector compared to the western part. Given that skillful seasonal forecasting of equatorial rainfall has critical socio-economic implications including reservoir management, groundwater recharge, irrigation planning, and agricultural productivity these findings provide valuable guidance for policymakers in the region to strengthen adaptation strategies and risk mitigation efforts.

Acknowledgements The authors thank you to all reanalysis, observational, satellite and hindcast data providers used in this study. We would like to express our gratitude to the anonymous reviewers, along with the editor for their constructive suggestions, which have greatly improved the quality of the paper. We gratefully appreciate the efforts of the International Joint Laboratory Dynamics of Terrestrial Ecosystems in Central Africa (IJL DYCOCA/ LMI DYCOFAC) initiative during the realisation of this work.

Code availability Figures shown in this study are plotted using the NCAR Command Language (NCL; https://doi.org/10.5065/D6WD3XH5, NCAR Command Language, 2017). Codes can be obtained from the corresponding author.

Author's contributions HNN: Conceptualization; data upload; data analysis; formal analysis; investigation; methodology; software; validation; writing-original draft; writing-review and editing. **RST:** Project administration; supervision; validation; methodology; writing; review and editing. **MG:** Project administration; supervision; investigation; validation; writing-original draft; writing-review and editing. **DAV:** Project administration; supervision; validation, methodology; writing; review and editing.

Funding Not applicable

Data availability All observational and reanalysis data used in this study are publicly available at no charge and with unrestricted access. The ERA5 reanalysis is produced within the Copernicus Climate Change Service (C3S) by the ECMWF and is accessible via the link https://cds.climate.copernicus.eu/datasets/; the CHIRPS2 data are available at https://data.chc.ucsb.edu/products/CHIRPS-2.0/global_daily/netcdf/; the ERSST data are available at https://iridl.ldeo.columbia.edu/SOURCES/.NOAA/.NCDC/.ERSST/.version5/. The ECMWF-SEAS5.1 model data can be downloaded from the Copernicus Climate Data Store (https://cds.climate.copernicus.eu/datasets/seasonal-monthly-pressure-levels?tab=download)

Conflict of interest The authors declare no conflicts of interest relevant to this study.

867 **References**

868 Abid, M. A., Kucharski, F., Molteni, F., and Almazroui, M.: Predictability of Indian Ocean
869 precipitation and its North Atlantic teleconnections during early winter, npj
870 Clim Atmos Sci 6, 17 (2023), https://doi.org/10.1038/s41612-023-00328-z, 2022.
871 Attada, R., Ehsan, M. A., and Pillai, P. A.: Evaluation of potential predictability of
872 indian summer monsoon rainfall in ecmwf's fifth-generation seasonal forecast
873 system (SEAS5), Pure Appl. Geophys., 179(12), 4639–4655,
874 https://doi.org/10.1007/s00024-022-03184-9, 2022.
875 Behera, S. K., Luo, J.-J., Masson, S., Delecluse, P., Gualdi, S., Navarra, A., and Yamagata,
876 T.: Paramount impact of the Indian Ocean dipole on the East African short
877 rains: A CGCM study, J. Climate, 18(21), 4514–4530,
878 https://doi.org/10.1175/jcli3541.1, 2005.
879 Cai, W., van Rensch, P., Cowan, T., and Hendon, H. H.: Teleconnection pathways of
880 ENSO and the IOD and the mechanisms for impacts on australian rainfall, J.
881 Climate, 24(15), 3910–3923, https://doi.org/10.1175/2011jcli4129.1, 2011.
882 Cook, K. H., and Vizy, E. K.: Hydrodynamics of regional and seasonal variations in
883 Congo Basin precipitation, Clim. Dynam., 59(5–6), 1775–1797,
884 https://doi.org/10.1007/s00382-021-06066-3, 2021.
885 Dezfuli, A.: Climate of Western and Central Equatorial Africa. In Oxford Research
886 Encyclopedia of Climate Science. Oxford University Press,
887 https://doi.org/10.1093/acrefore/9780190228620.013.511, 2017.
888 Dezfuli, A. K., and Nicholson, S. E. : The relationship of rainfall variability in Western
889 Equatorial Africa to the tropical oceans and atmospheric circulation. Part II: The
890 Boreal Autumn, J. Climate, 26(1), 66–84,
891 https://doi.org/10.1175/jcli-d-11-00686.1, 2013.
892 Dinku, T., Funk, C., Peterson, P., Maidment, R., Tadesse, T., Gadain, H., and Ceccato, P.:
893 Validation of the CHIRPS satellite rainfall estimates over eastern Africa, Quart. J.
894 Roy. Meteorol. Soc., 144(S1), 292–312, https://doi.org/10.1002/qj.3244, 2018.
895 Ehsan, M. A., Tippett, M. K., Robertson, A. W., Almazroui, M., Ismail, M., Dinku, T.,
896 Acharya, N., Siebert, A., Ahmed, J. S., and Teshome, A.: Seasonal
897 predictability of Ethiopian Kiremt rainfall and forecast skill of ECMWF's SEAS5
898 model, Clim. Dynam., 57(11–12), 3075–3091,
899 https://doi.org/10.1007/s00382021-05855-0, 2021.
900 Feudjio Tchinda, A., Tanessong, R. S., Mamadou, O., Tchida Diffo, V., Djomou Yepdo, Z.,
901 and Chabi Orou, J. B.: Predictive skill of North American Multi-Model Ensemble
902 seasonal forecasts for the climate rainfall over Central Africa, Meteorol. Appl.,
903 29(3), https://doi.org/10.1002/met.2074, 2022.
904 Funk, C., Peterson, P., Landsfeld, M., Pedreros, D., Verdin, J., Shukla, S., Husak, G.,
905 Rowland, J., Harrison, L., Hoell, A., and Michaelsen, J.: The climate hazards

infrared precipitation with stations—a new environmental record for monitoring extremes, Sci. Data, 2(1), https://doi.org/10.1038/sdata.2015.66, 2015.
Gebrechorkos, S. H., Pan, M., Beck, H. E., and Sheffield, J.: Performance of state-of-the-art C3S european seasonal climate forecast models for mean and extreme precipitation over africa, Water Resour. Res., 58(3), https://doi.org/10.1029/2021wr031480, 2022.
Gleixner, S., Demissie, T., and Diro, G. T.: Did ERA5 improve temperature and precipitation reanalysis over east africa? Atmosphere, 11(9), 996, https://doi.org/10.3390/atmos11090996, 2020.
Gudoshava, M., Nyinguro, P., Talib, J., Wainwright, C., Mwanthi, A., Hirons, L., de Andrade, F., Mutemi, J., Gitau, W., Thompson, E., Gacheru, J., Marsham, J., Endris, H. S., Woolnough, S., Segele, Z., Atheru, Z., and Artan, G.: Drivers of sub-seasonal extreme rainfall and their representation in ECMWF forecasts during the Eastern African March-to-May seasons of 2018–2020, Meteorol. Appl., 31(5), https://doi.org/10.1002/met.70000, 2024.
Gudoshava, M., Wainwright, C., Hirons, L., Endris, H. S., Segele, Z. T., Woolnough, S., Atheru, Z., and Artan, G.: Atmospheric and oceanic conditions associated with early and late onset for Eastern Africa short rains, Int. J. Climatol., 42(12), 6562–6578, https://doi.org/10.1002/joc.7627, 2022.
Gudoshava, M., Wanzala, M., Thompson, E., Mwesigwa, J., Endris, H. S., Segele, Z., Hirons, L., Kipkogei, O., Mumbua, C., Njoka, W., Baraibar, M., de Andrade, F., Woolnough, S., Atheru, Z., and Artan, G.: Application of real time S2S forecasts over Eastern Africa in the co-production of climate services, Clim. Services, 27, 100319, https://doi.org/10.1016/j.cliser.2022.100319, 2022.
Hersbach, H., Bell, B., Berrisford, P., Hirahara, S., Horányi, A., Muñoz-Sabater, J., Nicolas, J., Peubey, C., Radu, R., Schepers, D., Simmons, A., Soci, C., Abdalla, S., Abellan, X., Balsamo, G., Bechtold, P., Biavati, G., Bidlot, J., Bonavita, M., … Thépaut, J.: The ERA5 global reanalysis, Quart. J. Roy. Meteorol. Soc., 146(730), 1999-2049, https://doi.org/10.1002/qj.3803, 2020.
Huang, B., Thorne, P. W., Banzon, V. F., Boyer, T., Chepurin, G., Lawrimore, J. H., Menne, M. J., Smith, T. M., Vose, R. S., and Zhang, H.-M.: Extended reconstructed sea surface temperature, version 5 (ersstv5): Upgrades, validations, and intercomparisons, J. Climate, 30(20), 8179–8205, https://doi.org/10.1175/jcli-d-16-0836.1, 2017.
Husak, G. J., Michaelsen, J., and Funk, C.: Use of the gamma distribution to represent monthly rainfall in Africa for drought monitoring applications, Int. J. Climatol., 27(7), 935–944, https://doi.org/10.1002/joc.1441, 2006.
Ibebuchi, C. C.: Revisiting the 1992 severe drought episode in South Africa: The role of El Niño in the anomalies of atmospheric circulation types in Africa south of the equator, Theor. Appl. Climatol., 146(1–2), 723–740,

https://doi.org/10.1007/s00704-021-03741-7, 2021.
Ingeri, C., Wen, W., Sebaziga, J. N., Iyakaremye, V., Ekwacu, S., Ayabagabo, P., Twahirwa, A., and Kazora, J.: Potential driving systems associated with extreme rainfall across East Africa during october to december (OND) season 2019, Journal of Geoscience and Environment Protection, 12(07), 25–49, https://doi.org/10.4236/gep.2024.127003, 2024.
Johnson, S. J., Stockdale, T. N., Ferranti, L., Balmaseda, M. A., Molteni, F., Magnusson, L., Tietsche, S., Decremer, D., Weisheimer, A., Balsamo, G., Keeley, S. P. E., Mogensen, K., Zuo, H., and Monge-Sanz, B. M.: SEAS5: The new ECMWF seasonal forecast system, Geosci. Model Dev., 12(3), 1087–1117, https://doi.org/10.5194/gmd-12-1087-2019, 2019.
Kang, IS., and Shukla, J.: Dynamic seasonal prediction and predictability of the monsoon. In: The Asian Monsoon, Springer Praxis Books. Springer, Berlin, Heidelberg, https://doi.org/10.1007/3-540-37722-0_15, 2006.
Kenfack, K., Marra, F., Djomou, Z. Y., Tchotchou, L. A. D., Tamoffo, A. T., and Vondou, D. A.: Dynamic and thermodynamic contribution to the October 2019 exceptional rainfall in western central Africa, Weather Clim. Dynam., 5, 1457–1472, https://doi.org/10.5194/wcd-5-1457-2024, 2024.
Kolstad, E. W., and MacLeod, D. : Lagged oceanic effects on the East African short rains, Clim. Dynam., 59(3–4), 1043–1056, https://doi.org/10.1007/s00382-022-06176-6, 2022.
Kolstad, E. W., Parker, D. J., MacLeod, D. A., Wainwright, C. M., and Hirons, L. C.: Beyond the regional average: Drivers of geographical rainfall variability during East Africa's short rains, Quart. J. Roy. Meteorol. Soc., 150(764), 4550–4566, https://doi.org/10.1002/qj.4829, 2024.
Kuete, G., Pokam Mba, W., and Washington, R.: African Easterly Jet South: Control, maintenance mechanisms and link with Southern subtropical waves, Clim. Dynam., 54(3–4), 1539–1552, https://doi.org/10.1007/s00382-019-05072-w, 2019.
Longandjo, G.-N. T., and Rouault, M.: On the structure of the regional-scale circulation over Central Africa: Seasonal evolution, variability, and mechanisms, J. Climate, 33(1), 145–162, https://doi.org/10.1175/jcli-d-19-0176.1, 2020.
Longandjo, G.-N. T., and Rouault, M.: Revisiting the seasonal cycle of rainfall over Central Africa, *J. Climate*, *37*(3), 1015–1032, https://doi.org/10.1175/jcli-d-23-0281.1, 2024.
Moihamette, F., Pokam, W. M., Diallo, I., and Washington, R.: Response of regional circulation features to the Indian Ocean dipole and influence on Central Africa climate, Clim. Dynam., 62(6), 1–21, https://doi.org/10.1007/s00382-024-07251-w, 2024.

Mwangi, E., Wetterhall, F., Dutra, E., Di Giuseppe, F., & Pappenberger, F.: Forecasting droughts in East Africa, Hydrol. Earth Syst. Sci., 18(2), 611–620, https://doi.org/10.5194/hess-18-611-2014, 2014.

Nana, H. N., Gudoshava, M., Tanessong, R. S., Tamoffo, A. T., and Vondou, D. A.: Diverse causes of extreme rainfall in November 2023 over Equatorial Africa, Weather Clim. Dynam., 6(3), 741–756, https://doi.org/10.5194/wcd-6-741-2025

Nana, H. N., Tamoffo, A. T., Kaissassou, S., Djiotang Tchotchou, L. A., Tanessong, R. S., Kamsu-Tamo, P. H., Kenfack, K., and Vondou, D. A.: Performance-based evaluation of NMME and C3S models in forecasting the June–August Central African rainfall under the influence of the South Atlantic Ocean Dipole, Int. J. Climatol., 44(7), 2462–2483, https://doi.org/10.1002/joc.8463, 2024.

Nana, H. N., Tanessong, R. S., Tchotchou, L. A. D., Tamoffo, A. T., Moihamette, F., and Vondou, D. A.: Influence of strong South Atlantic Ocean Dipole on the Central African rainfall's system, Clim. Dynam., 62(1), 1–16, https://doi.org/10.1007/s00382-023-06892-7, 2023.

Nicholson, S. E.: Long-term variability of the East African 'short rains' and its links to large-scale factors, Int. J. Climatol., 35(13), 3979–3990, https://doi.org/10.1002/joc.4259, 2015.

Nicholson, S. E., and Grist, J. P.: The seasonal evolution of the atmospheric circulation over west africa and equatorial africa, J. Climate, 16(7), 1013–1030, https://doi.org/10.1175/1520-0442(2003)016<1013:tseota>2.0.co;2, 2003.

Okoola R. E., Camberlin P., and Ininda J. M. : Wet periods along the East African Coast and the extreme wet spell of October 1997, J. Kenya Meteorol. Soc., 2:67–83, ⟨hal-00320637⟩, 2008.

Palmer, P. I., Wainwright, C. M., Dong, B., Maidment, R. I., Wheeler, K. G., Gedney, N., Hickman, J. E., Madani, N., Folwell, S. S., Abdo, G., Allan, R. P., Black, E. C. L., Feng, L., Gudoshava, M., Haines, K., Huntingford, C., Kilavi, M., Lunt, M. F., Shaaban, A., and Turner, A. G.: Drivers and impacts of Eastern African rainfall variability, Nat. Rev. Earth Environ., 4(4), 254–270, https://doi.org/10.1038/s43017-023-00397-x, 2023.

Pokam, W. M., Bain, C. L., Chadwick, R. S., Graham, R., Sonwa, D. J., and Kamga, F. M. : Identification of processes driving low-level westerlies in west equatorial africa, J. Climate, 27(11), 4245–4262, https://doi.org/10.1175/jcli-d-13-00490.1, 2014.

Pokam, W. M., Djiotang, L. A. T., and Mkankam, F. K.: Erratum to: Atmospheric water vapor transport and recycling in Equatorial Central Africa through NCEP/NCAR reanalysis data, Clim. Dynam., 42(1–2), 553–553, https://doi.org/10.1007/s00382-013-1977-4, 2013.

Preethi, B., Sabin, T. P., Adedoyin, J. A., and Ashok, K.: Impacts of the ENSO Modoki

and other Tropical Indo-Pacific Climate-Drivers on African Rainfall, Sci. Rep., 5(1), https://doi.org/10.1038/srep16653, 2015.
Rowell, D. P., Folland, C. K., Maskell, K., and Ward, N. M.: Variability of summer rainfall over tropical north Africa (1906-92): Observations and modelling, Quart. J. Roy. Meteorol. Soc., 121(523), 669–704, https://doi.org/10.1256/smsqj.52310, 1995.
Roy, I., and Troccoli, A.: Identifying important drivers of East African October to December rainfall season, Sci. Total Environ., 914, 169615, https://doi.org/10.1016/j.scitotenv.2023.169615, 2024.
Saha, S., Moorthi, S., Wu, X., Wang, J., Nadiga, S., Tripp, P., Behringer, D., Hou, Y.-T., Chuang, H., Iredell, M., Ek, M., Meng, J., Yang, R., Mendez, M. P., van den Dool, H., Zhang, Q., Wang, W., Chen, M., and Becker, E.: The NCEP climate forecast system version 2, J. Climate, 27(6), 2185–2208, https://doi.org/10.1175/jcli-d-12-00823.1, 2014.
Saji, N. H., Goswami, B. N., Vinayachandran, P. N., and Yamagata, T.: A dipole mode in the tropical Indian Ocean, Nature, 401(6751), 360–363, https://doi.org/10.1038/43854, 1999.
Tanessong, R. S., Fotso-Nguemo, T. C., Kaissassou, S., Guenang, G. M., Komkoua Mbienda, A. J., Djiotang Tchotchou, L. A., Tchinda, A. F., Vondou, D. A., Pokam, W. M., Igri, P. M., and Yepdo, Z. D.: Climate forecast skill and teleconnections on seasonal time scales over Central Africa based on the North American Multi-Model Ensemble (NMME), Meteorol. Atmos. Phys., 136(3). https://doi.org/10.1007/s00703-024-01018-y, 2024.
Tanessong, R. S., Igri, P. M., Vondou, D. A., Tamo, P. H. K., and Kamga, F. M.: Evaluation of probabilistic precipitation forecast determined from WRF forecasted amounts, Theor. Appl. Climatol., 116(3–4), 649–659, https://doi.org/10.1007/s00704-013-0965-2, 2013.
Tanessong, R. S., Vondou, D. A., Djomou, Z. Y., and Igri, P. M.: WRF high resolution simulation of an extreme rainfall event over Douala (Cameroon): A case study, Model, Earth Syst. Environ., 3(3), 927–942, https://doi.org/10.1007/s40808-017-0343-7, 2017.
Tefera, A. K., Liguori, G., Cabos, W., and Navarra, A.: Seasonal forecasting of East African short rains, Sc. Rep., 15(1), https://doi.org/10.1038/s41598-025-86564-0, 2025.
Trenberth, K. E.:The definition of El Niño, Bull. Amer. Meteorol. Soc., 78(12), 2771–2777, https://doi.org/10.1175/1520-0477(1997)078<2771:tdoeno>2.0.co;2, 1997.
Wilks, D. S.: "The Stippling Shows Statistically Significant Grid Points": How Research Results are Routinely Overstated and Overinterpreted, and What to Do about It, Bull. Amer. Meteorol. Soc., 97(12), 2263–2273, https://doi.org/10.1175/bams-d-15-00267.1, 2016.